2009

Thermal perturbations caused by large impacts and consequences for mantle convection

Wesley Andres Watters
wwatters@wellesley.edu

M. T. Zuber

B. H. Hager

Recommended Citation

Watters, W. A., M. T. Zuber, and B. H. Hager (2009), Thermal perturbations caused by large impacts and consequences for mantle convection, J. Geophys. Res., 114, E02001, doi:10.1029/2007JE002964.

Thermal perturbations caused by large impacts and consequences for mantle convection

W. A. Watters,[1] M. T. Zuber,[1] and B. H. Hager[1]

Received 8 July 2007; revised 17 July 2008; accepted 15 August 2008; published 4 February 2009.

[1] We examine the effects of thermal perturbations on a convecting layer of incompressible fluid with uniform viscosity in the limit of infinite Prandtl number, for two upper boundary conditions (free- and no-slip) and heat sources (100% volumetric heating and 100% bottom heating) in 2-D Cartesian finite element simulations. Small, low-temperature perturbations are swept into nearby downflows and have almost no effect on the ambient flow field. Large, high-temperature perturbations are rapidly buoyed and flattened, and spread along the layer's upper boundary as a viscous gravity current. The spreading flow severs and displaces downwellings in its path, and also thins and stabilizes the upper thermal boundary layer (TBL), preventing new instabilities from growing until the spreading motion stops. A return flow driven by the spreading current displaces the roots of plumes toward the center of the spreading region and inhibits nascent plumes in the basal TBL. When spreading halts, the flow field is reorganized as convection reinitiates. We obtain an expression for the spreading time scale, t_s, in terms of the Rayleigh number and a dimensionless perturbation temperature (Θ), as well as a size (Λ), and a condition that indicates when convection is slowed at a system-wide scale. We also describe a method for calculating the heat deposited by shock waves at the increased temperatures and pressures of terrestrial mantles, and supply estimates for projectile radii in the range 200 to 900 km and vertical incident velocities in the range 7 to 20 km s^{-1}. We also consider potential applications of this work for understanding the history of early Mars.

Citation: Watters, W. A., M. T. Zuber, and B. H. Hager (2009), Thermal perturbations caused by large impacts and consequences for mantle convection, *J. Geophys. Res.*, *114*, E02001, doi:10.1029/2007JE002964.

1. Introduction

[2] Collisions of large planetary bodies are thought to have played a central role in the formation and thermal evolution of the terrestrial planets and moons. Apart from their role in planetary accretion [*Wetherill*, 1990], the largest collisions might have caused resurfacing on a global scale [*Tonks and Melosh*, 1993]. Long after the formation of the terrestrial planets, smaller collisions had a major influence on the evolution of planetary interiors.

[3] Much recent attention has focused on the possibility that impacts initiate volcanism, and several mechanisms have been offered. A handful of studies have tried to relate impacts to volcanism occurring at large distances. It was suggested by *Schultz and Gault* [1975] that the focusing of seismic waves following an impact can cause disruption of antipodal terrains, and *Williams and Greeley* [1994] proposed that fractures formed in this manner can serve as conduits for magmas.

[4] Most work has focused on volcanism in the immediate vicinity of impacts. It was long ago suggested that the collapse of large complex craters can cause the uplift of upper mantle rocks that melt upon decompression [*Green*, 1972]. The distances involved in this uplift are possibly too small, however, to provoke widespread melting [*Ivanov and Melosh*, 2003]. A related mechanism emphasizes the overburdern pressure drop caused by crater excavation, expected to initiate instantaneous decompression melting of a small volume in the upper mantle (comparable to the excavation volume) beneath a thin lithosphere [*Green*, 1972; *Jones et al.*, 2002; *Elkins-Tanton and Hager*, 2005]. Subsequent relaxation of the lithosphere and the anomalous partial melt buoyancies can lead to upwelling of additional material that melts upon decompression, forming a long-lived shallow mantle plume.

[5] A few studies have suggested that impacts can initiate deep mantle plumes. *Abbott and Isley* [2002] find a correlation between the ages of major impacts and episodes of plume-initiated volcanism in the terrestrial geologic record. A causal mechanism was suggested by *Muller* [2002], in which avalanches at the core-mantle boundary (CMB) are triggered by the high shear stresses imparted in highly oblique impacts, exposing insulated regions of the D'' layer to core heating. Leaving aside the formidable problem of relating deep mantle plumes to a Chicxulub-scale event, time scales for plume ascent are too long to reconcile this

[1]Department of Earth, Atmospheric, and Planetary Sciences, Massachusetts Institute of Technology, Cambridge, Massachusetts, USA.

0148-0227/09/2007JE002964

impact with the flood basalts of the Deccan Traps [*Loper*, 1991].

[6] The evolution of large partial and total melt volumes generated by giant impacts was addressed more recently by *Reese et al.* [2004] and *Reese and Solomatov* [2006]. The former study estimates the volume of magmatic construction that results from a long-lived shallow mantle plume initiated by a large impact on Mars, obtaining volumes comparable to the total volume of the Tharsis rise. The latter study [*Reese and Solomatov*, 2006] employs a suite of analytical models and scaling arguments to estimate the time scales associated with different stages of the evolution, such as differentiation, crystallization, dynamic adjustment, and lateral spreading of the melt volume. The authors find that giant impacts can form extensive magma oceans which upon cooling exhibit crustal thickness variations similar to what is observed for the hemispheric dichotomy on Mars. Still more recently, a cooling viscous drop model was used by *Monteux et al.* [2007] to obtain the time and length scaling for the dynamic adjustment of impact-related thermal anomalies in the absence of ambient fluid motion, for the case of large impacts on bodies ranging in size between the Moon and Mars.

[7] A number of studies have addressed a possible link between impacts and the mare basalts that flooded large basins on the moon. *Manga and Arkani-Hamed* [1991] proposed that high-porosity ejecta blankets, by insulating the radiogenic KREEP layer, can trap enough heat to generate the lunar mare. To explain the absence of mare in the large South Pole-Aitken (SPA) basin, *Arkani-Hamed and Pentecost* [2001] examined the flattening and spreading of an impact-heating anomaly associated with basins of Imbrium and SPA size. In their numerical simulations, the KREEP layer was completely swept away by the spreading motion for SPA-sized impacts and not for those Imbrium-sized. With the aim of explaining the volume, late onset, and longevity of mare basalt volcanism, *Ghods and Arkani-Hamed* [2007] added impact-heating perturbations to a model lunar mantle (an unstable layer that was initially not convecting) and claimed that whole mantle convection and its consequences were an outcome of the perturbations. It should be noted, however, that impacts could not have induced whole mantle convection in young terrestrial mantles that were already convecting, and neither will buoyancy perturbations have this consequence in numerical models of a convecting layer.

[8] In the present study we examine how thermal buoyancy perturbations can disrupt and reorganize circulation in a convecting layer as well as obtain the time scaling of this interaction. We have added thermal perturbations to quasi steady state finite element solutions of the governing equations for subsolidus convection, for the case of an incompressible fluid in the limit of infinite Prandtl number, uniform viscosity, and a 2-D Cartesian geometry. In section 2 we summarize a method for calculating the amount of heat deposited deep in terrestrial mantles by the shock waves emanating from large impacts, where the increasing pressure and density with depth are taken into account. In sections 3 and 5 we use the results from section 2 and the estimated thermal structure of terrestrial mantles to construct thermal perturbations for use in our convection simulations. Perturbations of type I (section 3) are formed by truncating the shock-heating profile at a model solidus, and perturbations of type II (section 5) are formed by raising temperatures uniformly by a constant amount over a semicircular region. Section 4 contains a qualitative description of general features of the postimpact-heating evolution following perturbations of type I, based on time-lapse snapshots of the temperature and velocity fields. In section 6 we discuss the results of a large number of simulations with perturbations of type II, used to obtain an expression for the time scale of dynamic adjustment: the "spreading time scale," t_s. In section 7 we supply the conditions under which convection is dramatically slowed and the circulation pattern reorganized at a global scale. Section 8 contains a discussion of the implications of these results for alternative convection models, including other rheologies and three-dimensional domains. Finally, in section 9 we consider potential applications of our work for understanding the history of early Mars.

2. Shock Heating of Terrestrial Mantles

[9] A projectile incident at velocities typical of planetary collisions will cause a supersonic stress wave (a shock wave) to propagate through the target and projectile. A shock accelerates the material through which it passes to the particle velocity, u, while the shock front travels at a speed U. The pressure P, specific volume V, specific internal energy E, of the compressed material are related to uncompressed values (E_0, V_0, P_0) and the particle and front velocities in the Hugoniot equations [*Melosh*, 1989]

$$\rho(U-u) = \rho_0 U \tag{1}$$

$$P - P_0 = \rho_0 u U \tag{2}$$

$$E - E_0 = (P + P_0)(V_0 - V)/2 \tag{3}$$

where $\rho_0 = 1/V_0$ and $\rho = 1/V$. For mantle rocks, the experimentally determined Hugoniot curve (shock equation of state) in U-u space is well described by a linear relationship between shock and particle velocities

$$U = C + Su \tag{4}$$

where C is roughly the speed of sound at STP.

[10] Target materials are shocked to an approximately uniform peak shock pressure P_c within the isobaric core (IC) radius, r_c. Outside of this region, peak shock pressure P_s decays as an inverse power law of the radial distance r from the site of impact [*Ahrens and O'Keefe*, 1977]:

$$P_s = P_c(r_c/r)^n \tag{5}$$

Using the Sandia 2-D axisymmetric hydrocode CSQ, *Pierazzo et al.* [1997] found good agreement among decay law exponents for a wide range of materials. Fitting to results for iron, granite, and dunite (among others), *Pierazzo et al.* [1997] measured for n

$$n = (-1.84 \pm 0.17) + (2.61 \pm 0.14)\log v_i, \tag{6}$$

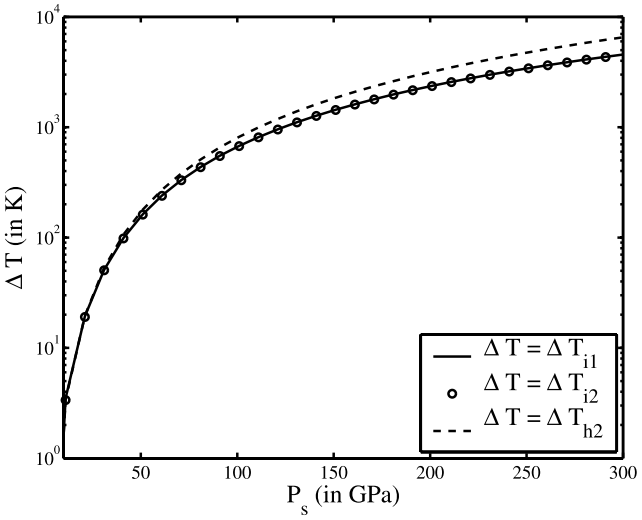

Figure 1. Shock heating calculated using three methods described in section 2 of the auxiliary material versus peak shock pressure P_s. (Assuming lower mantle properties, e.g., $S = 1.25$, $C = 7.4$ km s^{-1}; see section 3 of the auxiliary material.) The subscripts i1 and i2 refer to "isentrope release" methods (adiabatic decompression) and h2 refers to the "Hugoniot release" method summarized in the text and detailed in section 2 of the auxiliary material.

where v_i is the vertical incident velocity in km s^{-1}. We designate the exponents for the steepest, average, and most gradual decay laws as follows:

$$n_+ \equiv (-1.84 + 0.17) + (2.61 + 0.14) \log v_i \tag{7}$$

$$n_0 \equiv -1.84 + (2.61) \log v_i \tag{8}$$

$$n_- \equiv (-1.84 - 0.17) + (2.61 - 0.14) \log v_i \tag{9}$$

(An alternative decay law and other scaling relations used from *Pierazzo et al.* [1997] are discussed in section 1 of the auxiliary material.)[1]

[11] The internal energy of the shock state may be calculated using equation (3). Decompression converts much of the internal energy of the shock state into mechanical energy. Using elementary thermodynamic relations we can estimate the waste heat assuming that decompression follows the release isentrope, and these methods are described in section 2 of the auxiliary material. This involves first calculating the temperature of a given shock state along the Hugoniot, and then the temperature after decompression along the release isentrope.

[12] *Gault and Heitowit* [1963] derived a simple estimate of the waste heat ΔE_w, in which the shocked material is assumed to unload along a thermodynamic path that is approximated by the Hugoniot. This relation is derived by integrating the Hugoniot from the shock state to the release state in P-V space, and subtracting this from the shock state energy (equation (3)). (Assuming a linear shock EOS (equation (4)) and using the first two Hugoniot equations (1)–(2), one readily obtains the Hugoniot in P-V space.) This waste heat estimate is divided by the specific heat at constant pressure C_p to estimate the temperature increase ΔT_s caused by the shock. In the work by *Gault and Heitowit* [1963], ΔE_w is written in terms of the particle velocity u. We derive an alternative form in terms of the shock-increased pressure $P_\delta = P_s - P_0$ (for peak shock pressure P_s)

$$\Delta T_s(P_\delta) = \frac{P_\delta}{2\rho_0 S}\left(1 - f^{-1}\right) - (C/S)^2[f - \ln F - 1] \tag{10}$$

where

$$f(P_\delta) \equiv -\frac{P_\delta}{\beta}\left(1 - \sqrt{\frac{2P_\delta}{\beta} + 1}\right)^{-1} \tag{11}$$

and

$$\beta \equiv \frac{C^2 \rho_0}{2S} \tag{12}$$

where $\rho_0 = 1/V_0$ is the density prior to shock compression, corresponding to P_0. The principal advantage of this method is expedience, since we can avoid the numerical integrations required for the isentrope release methods. The amount of shock heating as a function of peak shock pressure is shown in Figure 1 for three methods described in section 2 of the auxiliary material, where the subscripts i1 and i2 refer to isentrope release and h2 refers to the result from equation (10). Equation (10) overestimates the amount of shock heating by roughly 20% at 125 GPa (1000 K), and 10% at 50 GPa (~100 K). The thermal perturbations that we construct in section 3 are limited by the solidus temperature, which is not estimated ever to exceed mantle geotherms by much more than 1000 K. Because shock heating decays rapidly with depth in the mantle (for large shock pressures), the net effect of this error is to overestimate the characteristic size of our perturbations by at most 200 km.

[13] As a shock wave propagates into the mantle of a terrestrial planet, the density and pressure of the unshocked target material increase with depth. Moreover, a Hugoniot centered at higher densities and pressures is different from one centered at STP for the same material. In order to estimate the shock heating, therefore, we require reference models of pressure and density for the two cases considered in this study: the Earth and Mars. For both planets we assume a single chemically homogeneous layer with mantle properties (the consequences of adding an upper mantle layer are considered in section 6 of the auxiliary material). The reference model for pressure is constructed from a Hugoniot-referenced compression isentrope, using the shock equation of state (EOS) obtained by *McQueen* [1991] for lower mantle rocks (for Earth models), and dunite and peridotite (for Mars models). The reference models for density are given by the adiabatic compression. A detailed account of how these models were assembled is supplied in section 3 of the auxiliary material.

[14] A simple approach for estimating shock temperature with depth is to calculate the shock heating from equation (10), while substituting for P_δ the difference

[1] Auxiliary materials are available in the HTML. doi:10.1029/2007JE002964.

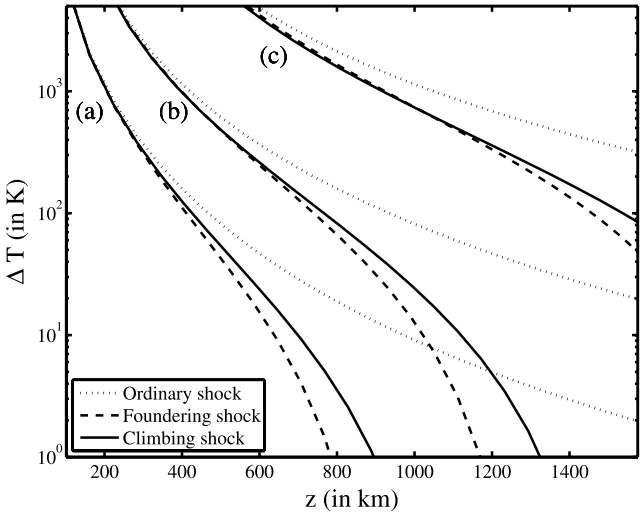

Figure 2. Shock heating as a function of depth for projectiles with a range of sizes, vertically incident at 15 km s^{-1}, for the case of the Mars-C reference model (see sections 3–5 of the auxiliary material). The shock pressure decay law exponent is $n = n_0$. (a) R = 50 km, (b) R = 100 km, and (c) R = 250 km.

between expected peak shock pressures from equation (5) and the ambient lithostatic pressure (from reference models). This approach is somewhat simplistic, however, since we have not totally accounted for the effect of increasing density. That is, the starting density ρ_0 in equation (10) is a function of depth. Even once this correction is made, we must account for changes in the Hugoniot as the starting pressure and density increase.

[15] As mentioned, the Hugoniot of a material shocked from a state (ρ_0, P_0) is not the same as the Hugoniot of the same material when shocked from (ρ_1, P_1) where $P_1 > P_0$ and $\rho_1 > \rho_0$. This problem is addressed in detail in section 5 of the auxiliary material. In outline, our approach is to divide the mantle into a stack of thin layers of increasing density, whose interfacial pressures also increase with depth. For each layer we obtain a Hugoniot centered upon its density. We invoke the planar impact approximation (see section 4 of the auxiliary material) and calculate the impedance match solution for the peak pressure of shocks transmitted through each layer. Within each layer, peak shock pressure is assumed to decay according to equation (5). In this way, we obtain the shock pressure and shock heating with depth. (Because the Hugoniot climbs the compression isentrope with increasing depth, these are called "climbing shocks," whereas estimates obtained by simply substituting the difference between P_s (from equation (5)) and lithostatic pressure for P_δ and reference model densities (section 3 of the auxiliary material) for ρ_0 in equation (10), are called "foundering shocks". Finally, estimates using equation (10) with equation (5) substituted for P_s without accounting for lithostatic pressure are called "ordinary shocks.")

[16] Shock heating estimates obtained by these methods are plotted in Figure 2. From this it is clear that the effect of lithostatic pressure is very important, while the difference between climbing and foundering shock estimates is negligible. A detailed discussion of the methods used to obtain these estimates for ΔT_s is contained in section 5 of the auxiliary material. One of the principal conclusions of this work is that the range in shock pressure decay exponents computed by *Pierazzo et al.* [1997] accounts for a range of shock-heating estimates that exceeds the errors associated with using the Hugoniot release or foundering shock approximations discussed above.

3. Convection Model Perturbations I

[17] We turn now to constructing thermal perturbations caused by shock heating for use in 2-D finite element simulations of mantle convection. We consider two kinds of perturbations. In the first case (type I perturbations), the anomaly is constructed according to the shock heating versus depth profiles calculated in section 2, where temperatures are set equal to the solidus temperature wherever this value is exceeded. This requires a model of the thermal structure of the mantle, which is discussed later in this section. We use this kind of perturbation, which has a realistic shape, to probe general features of the perturbation-driven flow in section 4. In the second case (type II perturbations, discussed in section 5), we raise mantle temperatures by a uniform amount throughout a semicircular region (with no imposed solidus ceiling). For that case we quantify the time scales of dynamic adjustment (section 6) in terms of the characteristic perturbation temperature and size. The simpler type II anomaly was used so that our results can be generalized more easily. Later, in sections 5 and 7, we make explicit the relationship between these types.

[18] In order to construct type I perturbations, we calculate the shock heating as a function of distance r from the IC center along rays oriented at an angle ϕ from the vertical. The IC is centered at a depth, d_c, according to the law supplied by *Pierazzo et al.* [1997] (see section 1 of the auxiliary material). We calculate shock heating along the rays for $\phi > 0$ by replacing z in the density profile (equation (25) in section 3 of the auxiliary material) with (d_c + $r\cos\phi$). In this way, the density profile (and the corresponding pressure profile) is "stretched" as a function of r as the angle ϕ increases. In calculating the climbing shock estimates for ΔT_s, we therefore obtain a 2-D function $\Delta T_s = f(r, \phi)$. A 2-D linear interpolation is used to construct the perturbation for regularly spaced cells in a rectilinear coordinate system $\Delta T_s = g(x, z)$. Shock heating in the near-surface region is complicated by the interference of decompression waves: we do not expect our estimates to be realistic in this zone.

3.1. Melt Volume and Model Assumptions

[19] Temperatures at the highest shock pressures considered in this study reach upward of 10^4 K, exceeding the temperatures at which vaporization is expected. Vaporization, crater excavation, and crater collapse dominate the evolution at short times near the planet surface and are not addressed in this study. We do not address the contribution of melt generated by the release of overburden pressure during and following the excavation process [*Jones et al.*, 2002]. Neither do we consider the processes associated with melt extraction or the decompression melting of shock-heated, upwelling mantle rocks. The dynamical consequences of differentiation are also ignored. The anomalous density of type I perturbations is due entirely to thermal expansion from shock-deposited heat. The shock-augmented

temperature is set equal to the local solidus temperature, T_m, wherever this value is exceeded.

[20] Some of the reasons for this choice are physical and some are practical in nature. First, regions that are raised to the liquidus temperature are apt to dissipate heat by convection and cool rapidly into partial melts on time scales that are short when compared with the time scales of subsolidus convection. *Reese and Solomatov* [2006] estimated that the time scale associated with crystallization of a total melt volume (spanning the mantle depth) down to a 40% melt fraction (the transition from crystal suspension to partially molten solid) would take a mere 300 to 1000 years. Cooling to solidus would require an additional 100 to 300 Ma if surface recycling occurs (Newtonian rheology), and much longer (up to 1 Ga) if a stagnant lid forms over the melt volume [*Reese and Solomatov*, 2006]. The former time scale (100–300 Ma) is comparable to the shortest time scales of dynamic adjustment calculated in this study (i.e., for the largest Rayleigh numbers).

[21] Moreover, partial melts have a strongly temperature-dependent rheology. The convection models that we consider in this study are isoviscous and ammenable to fast computation, so that we cannot treat in a realistic fashion viscosity of the partial melt. The time scales of initial dynamic adjustment and subsequent spreading of the viscous gravity current are mainly determined by the subsolidus rheology outside of the partial melt volume, as well as the anomalous buoyancy of the partial melt. The time and length scaling that characterizes a spreading, cooling viscous drop are barely altered by strongly temperature-dependent viscosity with large viscosity contrasts [*Monteux et al.*, 2007].

[22] Our calculations of shock heating anticipate that temperatures reaching the solidus will span much of the mantle for large impacts. The perturbations considered in this study correspond to the smallest melt volumes addressed by *Reese and Solomatov* [2006], and for which the time scales of dynamic adjustment are large compared with the crystallization times, precluding the formation of large magma oceans.

[23] In reality, on time scales associated with melt percolation and differentiation, a large quantity of melt is extracted while the density of the mantle residuum is diminished. *Reese et al.* [2004] considered the effects of melt extraction by comparing the time scales associated with convection and melt percolation. The authors estimated that a characteristic density contrast of 2% is associated with 15% melt extraction and 3% melt retention (assumed for the impact-related buoyancy anomalies in their models). A two percent drop in density corresponds to a 1000 K temperature anomaly in our models (assuming an expansivity of 2×10^{-5} K^{-1}).

[24] An anomalous buoyancy that derives from a partial melt is likely to dissipate far less rapidly than an equivalent thermal buoyancy. In our models, the anomalous buoyancy of thermal perturbations rapidly diminishes while very hot materials are brought close to the upper boundary, whose temperature is fixed. The resulting high thermal gradients cause rapid heat loss through the upper boundary, so that much of the remaining flow is driven by a smaller anomalous buoyancy. Therefore, translating between partial melt buoyancies and equivalent thermal buoyancies is only approximately valid for the rapid "flattening" stage (rapid viscous relaxation), and not for the "spreading" stage (spreading viscous gravity current) of the postimpact evolution (see section 4).

3.2. Thermal Reference Models

[25] In section 4 we describe the numerical models used to solve for the evolution of temperature and velocity. The starting temperature field (before perturbations are added) is obtained by running our models until a statistical steady state is reached; that is, a solution in which the averaged mantle velocity through time has a constant distribution. The dimensionless geotherm (horizontally averaged temperature profile) obtained from this solution is used to construct type I perturbations, as described below.

[26] In order to enforce the upper bound on shock heating we require a model solidus $T_m(z)$. For the Earth, we use a solidus that is consistent with the upper bound reported by *Zerr et al.* [1998] for a pyrolitic lower mantle [*Stacey*, 1992]. For the relatively shallow Martian mantle we use the pressure parameterization by *Reese and Solomatov* [1999] of the peridotite solidus. It was demonstrated by *Schmerr et al.* [2001] that an iron-enriched Martian mantle solidus lies, on average, roughly 200 K below the peridotite solidus. It should be noted, however, that the uncertainty in Martian mantle geotherms is greater than 200 K.

[27] Heating associated with adiabatic compression does not occur in our convection models. We therefore subtract from $T_m(z)$ (the solidus) the additional temperature ΔT_{ad} contributed by the adiabatic gradient. This correction is applied from the base of the upper thermal boundary layer to the base of the mantle. The adiabatic gradient is obtained using equation (25) in section 3 of the auxiliary material, along the principal isentrope. We chose an interior temperature for Earth's mantle such that the maximum horizontally averaged temperature in the upper thermal boundary layer of our model lies just below the solidus ($\approx$1700 K). In the case of Mars, we have chosen 1700 K for the base of the thermal boundary layer, consistent with the basal lithosphere temperature of model geotherms reported by *Spohn et al.* [1998].

[28] Figure 3 contains two diagrams showing the horizontally averaged model geotherm $\langle T \rangle$, the solidus T_m and the solidus with the adiabatic gradient subtracted ($T_m - \Delta T_{\mathrm{ad}}$), for the case of Earth (Figure 3a) and Mars (Figure 3b). In the plots of Figure 4 we show the difference between this adjusted solidus T_m' and the geotherm $\langle T \rangle$, as well as the shock heating with depth calculated for an impact on the Earth (Figure 3a) and Mars (Figure 3b). (see Figure 3 caption for details of the projectile parameters). In Figure 5 we illustrate each step in the construction of a type I perturbation, where the top frame corresponds to a time-independent steady state temperature field. The middle frame shows the shock heating caused by an impact. The last frame shows the sum of the top and middle frames, where T = T_m' wherever this value was exceeded in the sum.

4. Evolution of the Shock-Heated Region

[29] In this section we supply a qualitative description of the postimpact evolution based on time-lapse snapshots of the temperature and velocity fields following the insertion

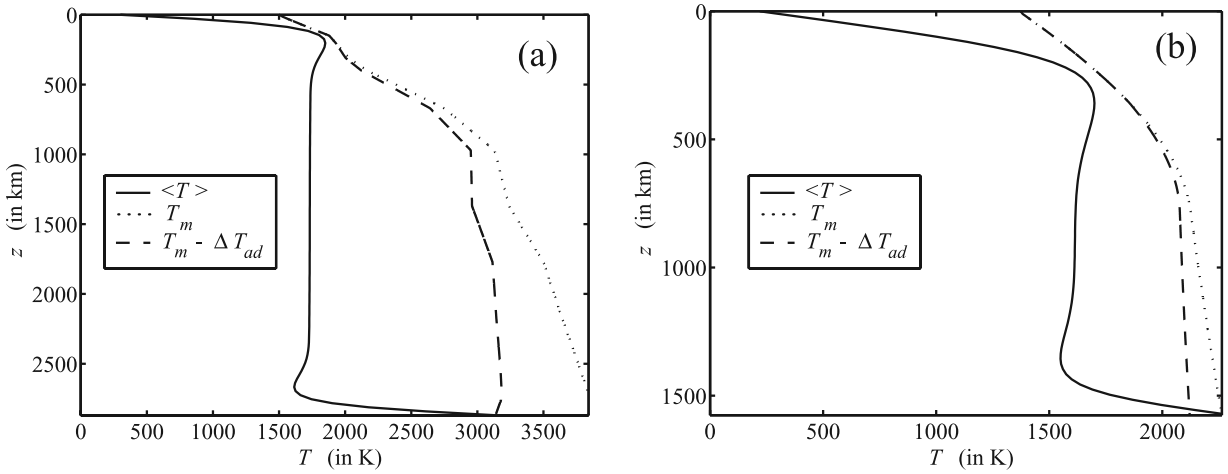

Figure 3. Thermal structure of (a) an Earth-like planet and (b) a Mars-like planet, assumed for constructing type I perturbations. The solid line indicates horizontally averaged mantle temperature $\langle T \rangle$ of a convection model calculation carried to quasi steady state (in Figure 3a $Ra = 7.5 \times 10^5$, stress-free upper boundary, fixed lower boundary temperature with no internal heating, in Figure 3b $Ra = 1.5 \times 10^5$, no-slip upper boundary, fixed lower boundary temperature with no internal heating). Also plotted is the solidus temperature T_m and "corrected" solidus temperature with the adiabatic gradient ΔT_{ad} subtracted. See text for discussion.

of type I perturbations. Solutions for temperature and velocity were obtained using finite element simulations of mantle convection for the case of an incompressible fluid in the limit of infinite Prandtl number. These were carried out using the 2-D Cartesian version of CONMAN [*King et al.*, 1990]. We have assumed a uniform viscosity in order to efficiently model the evolution for a large number of perturbation sizes, for different initial and boundary conditions and a range of Rayleigh numbers on large meshes.

[30] The aspect ratio of our mesh and domain is 1×6 for the calculations discussed in this section only, and 1×10 for the 8,000 calculations of section 6, where this is consistent with the estimated proportions of terrestrial mantles. The number of cells used in the vertical dimension was chosen so that thermal boundary layers were spanned by at least five cells in all cases. That is, for a calculation with $Ra = 1.0 \times 10^6$ we used a rectilinear mesh spanned by 120 elements in the vertical dimension, and 120×6 (this section) or 120×10 (section 6) elements in the horizontal dimension, all of them evenly spaced. Wraparound boundary conditions were imposed at the vertical bounding walls. By "100% bottom heating" we refer to models in which the temperatures of the upper and lower boundaries were fixed at constant values (i.e., not a lower-boundary heat flux

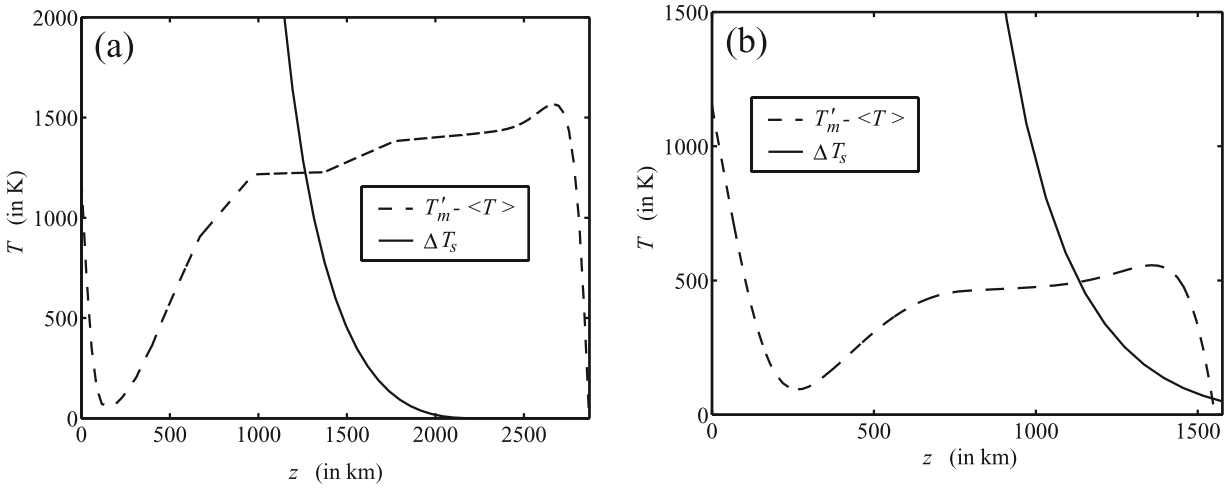

Figure 4. Shock heating ΔT_s with depth in the mantle of (a) an Earth-like planet caused by a projectile with radius $R = 600$ km and incident velocity 15 km s^{-1} and (b) a Mars-like planet (Mars-A; see Figure S3) caused by a projectile with radius $R = 375$ km and incident velocity 15 km s^{-1}. Peak shock pressure decays with exponent $n = n_0$. The adjusted solidus temperature T_m' minus the model geotherm $\langle T \rangle$ is plotted also. The perturbation temperature with depth directly beneath the impact is given by $T_m' - \langle T \rangle$ until it is crossed by ΔT_s and by ΔT_s below this depth.

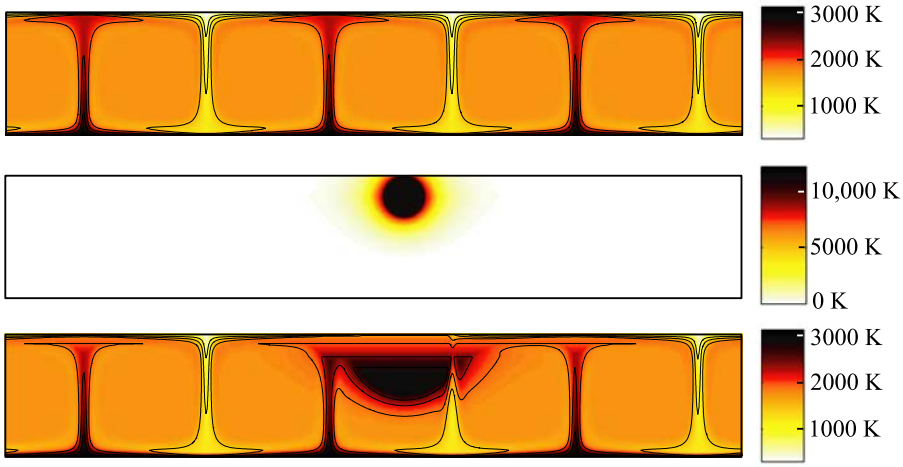

Figure 5. Construction of type I perturbations in two dimensions. The top shows a portion of the preimpact temperature field $T_0(x, z)$. The middle illustrates the temperature field calculated for shock heating ($\Delta T_s(x, z)$). The bottom shows the sum of these, where the temperature is set to $T_m'(z)$ (the local solidus temperature) at all points where $T_0 + \Delta T_s \geq T_m'$.

condition). Only the upper boundary temperature was fixed for calculations with 100% volumetric heating. Both upper and lower boundaries are impermeable. The dynamic Courant time step depends on the largest velocities in a given state of the system. The most important time scale in the perturbation-driven evolution, the spreading time scale (t_s), is typically spanned by 750 to 1500 program time steps.

[31] We begin with several caveats before describing the model results in detail. First, it should be emphasized that our calculations are carried out in two dimensions, so that instabilities which grow and detach from the basal thermal boundary layer (TBL) are neither plumes or the margins of rolls, where these latter structures are defined in terms of a three-dimensional geometry. Our convention is to refer to narrow upwellings as "plumes," and in section 8 we consider to what extent our results apply to the three-dimensional case.

[32] Second, the Rayleigh numbers for Earth-like models in this section are smaller than the Rayleigh number of whole mantle convection in the modern Earth, which is estimated to exceed 10^7 (i.e., an internal heating Rayleigh number). The value of *Ra* for the Earth's early mantle was larger still. In sections 6 and 7 we report on results for internal heating Rayleigh numbers comparable to modern values. We then assume these results hold for even larger values in order to estimate the consequences of large impacts for model mantles with values of *Ra* appropriate for the early solar system. Accurate calculations of convection on high aspect ratio meshes for very high Rayleigh numbers are outside the reach of our computational and temporal resources, since more mesh elements are required to resolve adequately the evolution of thermal boundary layers.

[33] For the simulations described in this section, the temperature of the lower boundary is fixed and there is no internal heating. This ensures a large temperature contrast for the basal TBL and a markedly unstable source layer for deep mantle plumes. Except for the interaction with plumes, general features of the evolution are very similar for the case of 100% volumetric heating, and for this reason we focus here on the bottom-heating case. The basal TBL for models in this section are spanned by a larger temperature contrast (as a fraction of the whole mantle convective driving temperature) than is considered realistic for the Earth's CMB.

[34] Numerous time-lapse snapshots of the temperature and velocity fields have been used to confirm that the fundamental processes described in this section for low *Ra* models operate in an identical fashion at higher *Ra*, although across different temporal and spatial scales. Convection models with 100% bottom heating at low Rayleigh numbers have the advantage that initial conditions are time-independent solutions of the governing equations. Changes in the temperature and velocity fields are therefore readily visible and can be assigned directly to the influence of the perturbation, which is less easily separated from the evolution of a time-dependent solution in which plumes and downwellings are constantly emerging and vanishing. The results in sections 6 and 7 are derived from a larger range in Rayleigh numbers, with internal heating and time-dependent initial conditions. We find that quantifiable properties of the evolution do not significantly depend upon whether the initial condition was time-dependent.

[35] The Martian mantle is thinner than Earth's mantle, so that impacts of the same energy will produce perturbations on a different scale with respect to layer thickness, in some cases heating the CMB directly. We do not consider the effects of solid state phase transformations, which occur within Mars at great depths and have been shown to diminish the number of large plumes in convection models [*Harder and Christensen*, 1996; *Breuer et al.*, 1998]. For the results reported in this section only, we enforce a stress-free upper boundary condition in the case of Earth-like models, and no-slip upper boundaries in the case of Mars-like models. The latter is an attempt to mimic the conditions of a stagnant lid, below which viscosity is approximately uniform [*Solomatov*, 1995].

4.1. Stages of the Postimpact Evolution

[36] The postimpact evolution for large-magnitude perturbations (i.e., large size and high temperature) observed in our models is summarized in Figure 6, and for a sample

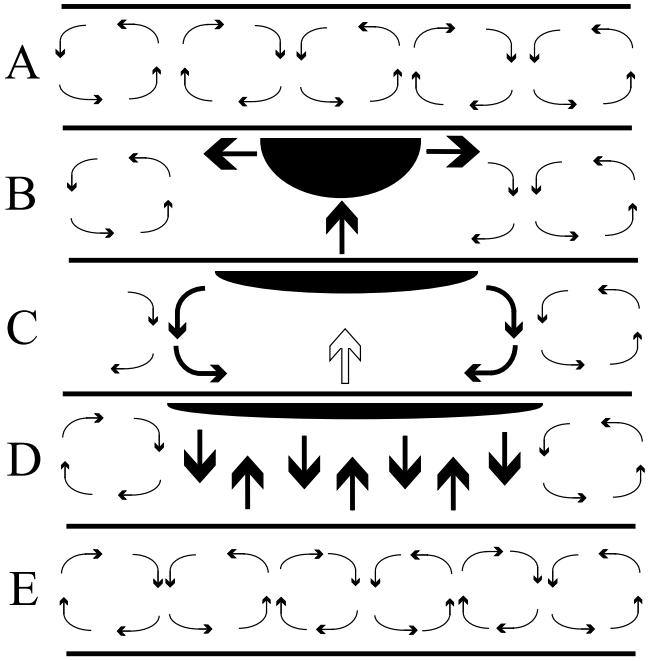

Figure 6. Principal stages in the evolution of the flow field following the insertion of large perturbations. (a) Preimpact convection pattern. (b) Flattening stage: vigorous buoyant ascent of the perturbation as it flattens on the time scale of viscous relaxation. (c) Spreading stage: the perturbation spreads along the top of the layer as a viscous gravity current, stabilizing the upper boundary. This motion drives a large-scale circulation pattern that also stabilizes the basal thermal boundary layer (TBL) and focuses flow below the center of the spreading region. In some cases this causes plume roots to coalesce into a megaplume. The flow decelerates throughout the spreading region as convection is stopped. (d) Recovery stage: the double-roll circulation pattern is maintained but stops expanding as the spreading current is halted by downwellings. Plumes and downwellings emerge in basal and upper TBLs as convection resumes and reorganizes the flow field. (e) The reorganized flow field at long time scales.

model calculation in Figure 7 (R = 600 km, v_i = 15 km s^{-1}, $n = n_0$; $Ra = 7.5 \times 10^5$, terrestrial mantle properties, and a stress-free upper boundary).

[37] 1. In the flattening stage, the buoyant region rises and flattens on the comparatively short time scale of viscous relaxation (Figure 6b, Figure 7, $t_1 < t < t_2$). The dynamics of the flattening stage are largely indifferent to the preimpact convection pattern. The flow brings high-temperature materials to the cold upper boundary in a relatively short time. The resulting large vertical temperature gradients, spanning a broad region of the upper boundary, cause rapid heat escape.

[38] 2. In the spreading stage, the substantially cooler anomaly then spreads along the upper boundary as a viscous gravity current (Figure 6c, Figure 7, $t_2 < t < t_4$). The spreading flow drives circulation in the layer over an expanding region, spanning the entire layer depth. This circulation creates a double-roll pattern with a weak central upwelling and marginal downwellings. (In three dimensions, this flow field would assume an annular shape.) Downwellings are destroyed when their source roots are sheared off by the spreading motion. Alternatively, the spreading current can displace an intact downwelling long distances, while its excess buoyancy is drained by the downwelling flow (Figure 7, leftward spreading current, frames t_3 and t_4), causing the current to slow down. The spreading motion, and simultaneous thinning of the upper thermal boundary layer (TBL) by the influx of hot material, stabilize the upper boundary against the formation of new instabilities and downwellings. This stabilizing effect and the destruction of downwellings stops convection and forms large zones of nearly stagnant flow (Figure 7, frame t_4).

[39] The spreading current also deflects plumes in its path, bending them in some cases parallel to the spreading motion. The upward flow in plumes that normally drains the basal thermal boundary layer is interrupted and slowed as a result. Meanwhile, the centrally directed return flow along the bottom of the mantle initially stabilizes the basal thermal boundary layer, which thickens while it is not being drained. The return flow along the base of the layer also pushes the roots of plumes close together, in some cases causing these to coalesce near the center of the spreading region. Shortly before the spreading motion halts, deflected plumes begin to right themselves and sometimes erode the spreading current, subtracting from the anomalous buoyancy driving its motion. New instabilities form in the basal TBL, inflate, and eventually detach as plumes.

[40] 3. Finally, the spreading motion is halted and the flow field is reorganized in the recovery stage (Figure 6d; Figure 7, $t_4 < t < t_7$). The fronts of the spreading current are stopped by downwellings, even while the pattern of motion (the double roll) remains largely intact. New downwellings emerge in the spreading region. A high concentration of plumes form in the spreading region also, where new plumes detach from inflating instabilities, and where the roots of old plumes have been pushed by the return flow. Convection has fully reinitiated and the flow pattern reorganizes.

[41] In the case of 100% bottom heating just described, the emergence of new downwellings in the spreading region can sometimes happen before the spreading motion halts. These downwellings emerge in zones of stagnating flow and where righted plumes have eroded through the blanket of hot material left behind by the spreading current. This enables the upper thermal boundary to recover locally, so that instabilities can emerge and inflate. The case of 100% volumetric heating differs in this regard, since the absence of plumes precludes them disrupting the spreading current. In all the cases that we have studied so far with 100% volumetric heating, downwellings in the spreading region do not emerge until after the spreading motion halts. Also, because of the spoke-like shape of plumes in three dimensions, this effect is unlikely to have the same importance for that geometry.

[42] The evolution of the temperature and velocity fields just described indicates two major episodes of magmatism characterized by very different source regions, spatial distributions, and time scales. The first has a highly uniform spatial distribution and broad extent, and occurs during the flattening and spreading stages. All of the material for this magmatic episode is derived from the perturbation itself, i.e., from shock-heated mantle rocks brought to the solidus by the flattening flow and distributed broadly by the

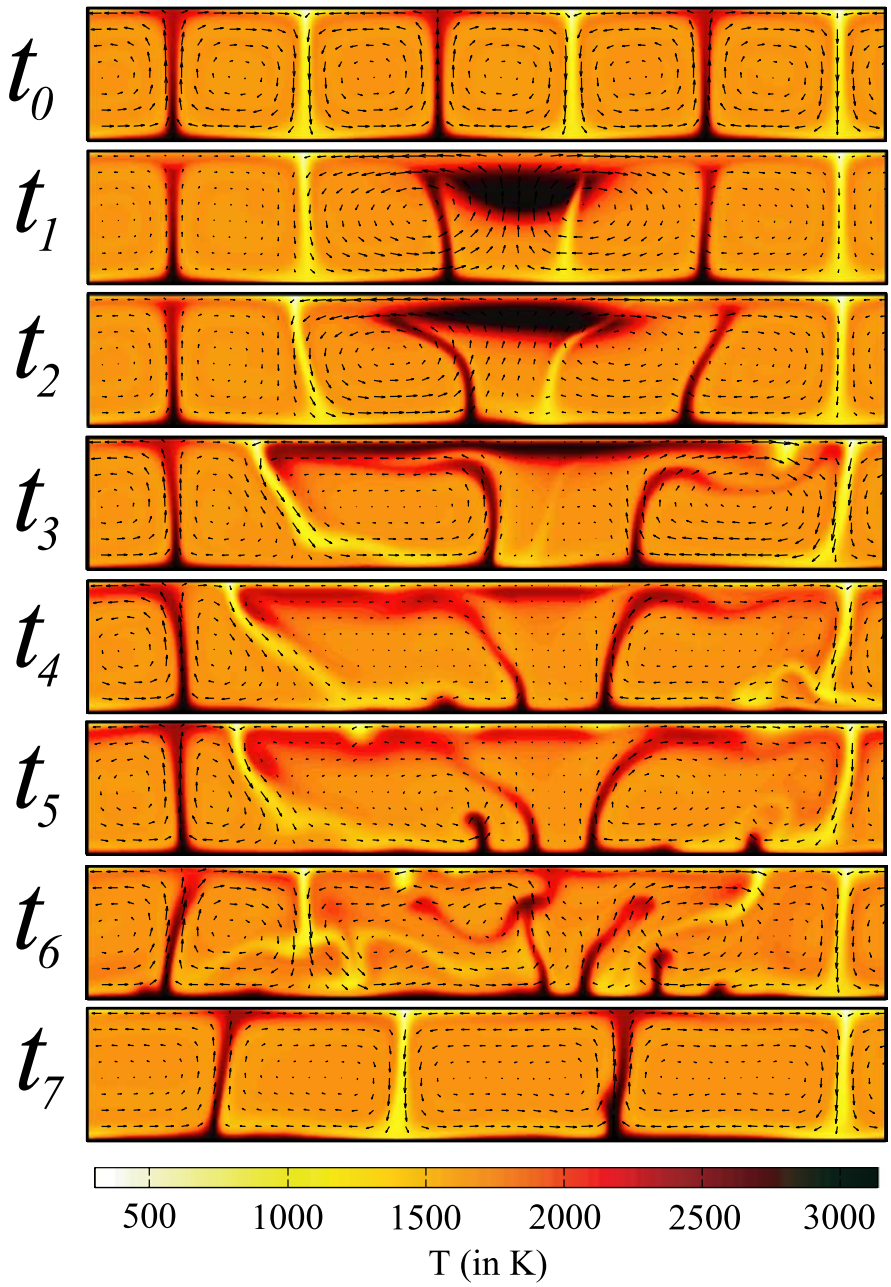

Figure 7. Evolution of the temperature and velocity fields for an Earth-like model (terrestrial mantle properties, stress-free upper boundary) and $Ra = 7.5 \times 10^5$ following insertion of a large-magnitude perturbation ($R = 600$ km, $v_i = 15$ km s^{-1}, $n = n_0$). Figure 4a shows the shock-heating profile for this case. The important features of the evolution are, frame-by-frame, as follows: $t_0 = 0$ Ma is the preimpact, steady state solution. $t_1 = 8$ Ma occurs during the flattening stage: double-roll pattern emerges as the perturbation flattens rapidly. At $t_2 = 50$ Ma, the perturbation begins to spread as a viscous gravity current along the upper boundary. Plumes and downwellings are deflected. At $t_3 = 225$ Ma, the leftward-spreading flow has encountered a downwelling, displacing it a long distance (intact). The excess buoyancy driving the front is drained by the downwelling flow, and the spreading motion slows. The rightward flow has severed a downwelling, and has displaced its root a long distance. The return flow along the bottom of the layer pushes the roots of plumes toward the center of the spreading region. At $t_4 = 550$ Ma, the hot spreading current and its return flow, by stabilizing both boundary layers, has caused large nearly stagnant zones to form in the spreading region. Plumes formerly deflected now right themselves, eroding the current and reducing further its driving buoyancy. The spreading motion slows down, and the basal return flow now fails to stabilize the basal TBL. Instabilities emerge and inflate. At $t_5 = 730$ Ma, downwellings and plumes emerge as the recovery stage begins. The frame corresponding to $t_6 = 1.6$ Ga shows the vigorous flow of the recovery stage as convection reorganizes. Note the high concentration of plumes near the center of the [former] spreading region. By $t_7 = 10$ Ga, the convection pattern has reorganized.

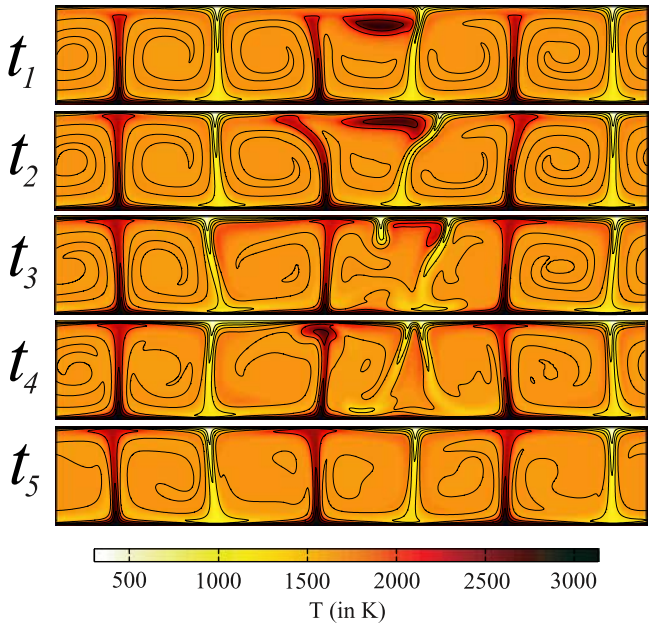

Figure 8. Evolution of the temperature field for the same convection model as shown in Figure 7, following an impact perturbation with the same incident velocity and $R = 300$ km (i.e., stress-free upper boundary terrestrial mantle dimensions and properties, $Ra = 7.5 \times 10^5$, $v_i = 15$ km s^{-1}, $n = n_0$). In this case, the perturbation-driven flow fails to reorganize the pattern and is quickly halted and drained by nearby downwellings. The times corresponding to each frame are $t_1 = 15$ Ma, $t_2 = 160$ Ma, $t_3 = 490$ Ma, $t_4 = 810$ Ma, and $t_5 = 3.8$ Ga. The spreading stage ended well before $t = 490$ Ma.

spreading flow. The second episode occurs in the recovery stage, as new downwellings and plumes emerge. In this stage, hot material deriving either from the basal TBL or the unshocked mantle are carried to the upper boundary by the vigorous motions of the reorganizing flow field. The magmatism associated with this event is likely to be localized spatially in pockets throughout the spreading region, occurring as sporadic episodes lasting for short times.

[43] For the calculation shown in Figure 7, the preimpact convection pattern is significantly reorganized by a perturbation with $R = 600$ km incident at $v_i = 15$ km s^{-1} (decay law exponent $n = n_0$). For the same incident velocity, perturbations resulting from projectile radii $R = 500$ km and $R = 400$ km also considerably alter the pattern by significantly displacing or breaching nearby downwellings. The case for $R = 300$ km (Figure 8), with the same convection model and incident velocity, fails to reorganize the preimpact flow field at long times, and the spreading flow is halted and drained by the nearest downwelling. The spreading time scale (the duration of the spreading stage) is noticeably shorter. Globally averaged mantle velocities are barely depressed in this case because no downwellings are destroyed. Still smaller perturbations make the transition from an advective mode of spreading to a diffusive mode before they are swept into nearby downflows.

[44] For a separate series of simulations the anomaly was centered on a downwelling, in a model mantle with Martian dimensions and a no-slip upper boundary, where $Ra = 10^5$. For incident velocity $v_i = 15$ km s^{-1} ($n = n_0$), only perturbations with $R > 250$ km succeeded in reorganizing the pattern. In section 7 we derive a condition, expressed in terms of perturbation magnitude, which indicates whether the flow field is significantly altered at a global scale, by predicting whether globally averaged mantle velocities will be depressed significantly.

[45] Finally, we explored the case of a marginally unstable layer, where $Ra = 5 \times 10^3$ for a mantle with Martian dimensions and a no-slip upper boundary. In this scenario, even very large impacts (e.g., $R = 500$ km, $v_i = 15$ km s^{-1}) fail to reorganize the circulation pattern. This is consistent with the condition that we derive in section 7, according to which the tendency for any convecting system to slow down at a global scale decreases with decreasing Ra for perturbations of a given magnitude. That is, the dissipative structures of low Ra convection are comparatively robust with respect to spatially localized perturbations. Note, however, that the change in Ra for this case is in effect due entirely to an increase in viscosity, while the applied driving temperature is held constant. Moreover, changes in projectile radius R for a constant incident velocity v_i mostly affect the size and not the temperature of the resulting perturbation. That is, for a constant characteristic perturbation temperature, expressed

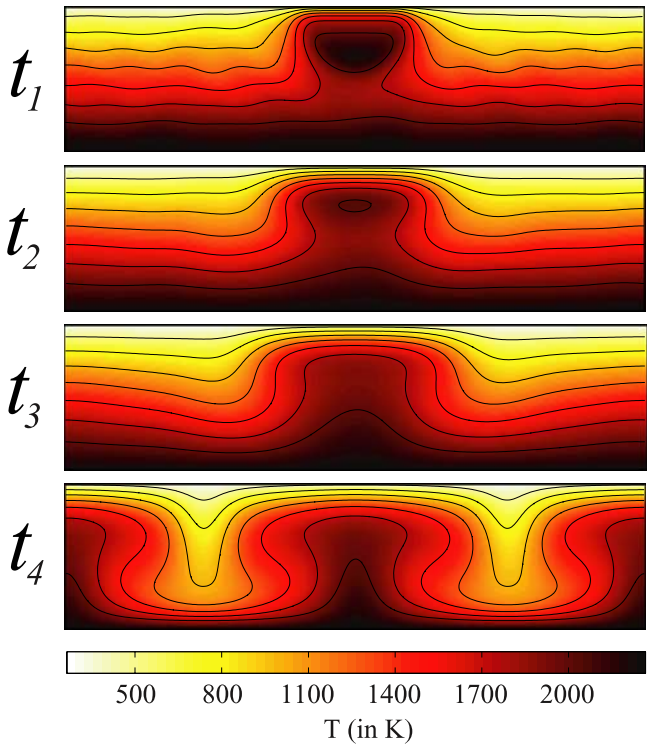

Figure 9. Evolution of a marginally unstable layer ($Ra = 5000$, no-slip upper boundary, Martian mantle properties) with weak spatially periodic thermal perturbations and a single impact perturbation ($R = 250$ km, $v_i = 15$ km s^{-1}, $n = n_0$). Adjustment of the perturbation establishes a long-lived plume, on which the long-term pattern is centered. Times corresponding to each frame are $t_1 = 110$ Ma, $t_2 = 550$ Ma, $t_3 = 1.1$ Ga, and $t_4 = 27.5$ Ga.

as a fraction of the whole mantle convective driving temperature, even the largest projectile radii (largest perturbations) which reorganized the pattern for high *Ra*, fail to do this for low *Ra* convection.

[46] Since convection is slow to begin from slight density heterogeneities in a marginally unstable layer, larger thermal perturbations control the long-term circulation pattern by fixing the location of long-lived plumes. In Figure 9 we show the results of a calculation in which a thermal anomaly was added to a marginally unstable layer with a conductive thermal profile, upon which weak, spatially periodic perturbations were also superposed. Unsurprisingly, the large perturbation organizes the flow field at long times.

4.2. Consequences for Deep Mantle Plumes

[47] There are several ways in which a thermal perturbation may directly or indirectly initiate, amplify, disrupt or suppress mantle plumes. Deep mantle plumes are focused upwellings of hot material that form within the unstable thermal boundary layer (TBL) at the base of terrestrial mantles. The discussion for the remainder of this section is informed by the results of numerical and laboratory studies of plume initiation [*Whitehead*, 1975; *Olson et al.*, 1987; *Bercovici and Kelly*, 1997; *Schubert et al.*, 2001]. The basal TBL is a hot, low-density layer overlain by a cool, higher-density mantle. A small local increase in thickness of the TBL results in a local decrease in density that drives upward flow. This upward flow increases the thickness of the TBL still further, resulting in a positive feedback, and therefore an instability: a protoplume. The protoplume grows in size as it is filled from below and as the TBL is drained, and can merge with other instabilities of similar size as they drift toward common density lows. The protoplume detaches if its Stokes ascent velocity exceeds the rate at which it is inflating.

[48] Linear stability analysis indicates that thermal boundary layers are stable with respect to small-amplitude perturbations if the local Rayleigh number Ra_δ does not exceed a critical value Ra_{cr} [*Howard*, 1966]. That is, the condition for stability is given by

$$Ra_\delta \equiv \frac{\alpha g \Delta T \delta^3}{\kappa \nu} \leq Ra_{cr} \tag{13}$$

where α is the thermal expansivity, g is the gravitational acceleration, δ is the local TBL thickness, κ is the thermal diffusivity, ΔT is the temperature contrast across the layer, and ν is the kinematic viscosity of the overlying mantle. This inequality does not, however, supply a complete picture of the conditions for plume formation, since it does not reflect the interaction with large-scale coherent motions in the mantle, which can tend to stabilize the upper and basal TBLs against the emergence and growth of Rayleigh-Taylor instabilities. From these considerations we can start to imagine how large thermal perturbations in the overlying mantle could suppress or initiate deep mantle plumes:

[49] 1. The shock waves can raise temperatures in the basal TBL or the lowermost mantle directly. This would lift TBL isotherms beneath the site of impact, with the potential of initiating buoyant perturbations in the layer (i.e., causing δ to increase locally, increasing Ra_δ). Moreover, heating of the lower mantle can lower the mantle viscosity ν (also increasing Ra_δ, and not addressed in our models).

[50] 2. In at least two ways, the perturbation-driven flow, directed away from the basal TBL (upward), might initiate a buoyancy perturbation in this layer. First, the ascending motion could lift isotherms and form a region of low density in the layer. Second, the ascending motion could directly entrain portions of the basal TBL. In this case, the rate of growth of a protoplume is driven by upward flow in the overlying mantle, and is faster than the relatively slow process of diapir inflation.

[51] 3. The large-scale anomaly driven circulation can increase the number and concentration of plumes by either one of two mechanisms. First, the return flow pushes the roots of plumes and nascent diapirs toward the center of the spreading region (i.e., toward a position beneath the site of impact). Second, the ascending motion above the basal TBL, by lifting basal isotherms, could create a local density low into which plumes and buoyant instabilities drift.

[52] 4. Finally, the large-scale anomaly driven circulation can suppress the formation of instabilities in two ways. First, the double-roll flow pattern set up by the flattening and spreading flow initially accelerates horizonal motions in the basal TBL, thereby shortening the mean residence time of the material in this layer. As this motion stalls when the spreading current is halted, the mean residence time increases, allowing instabilities to grow larger and detach as plumes. Second, the general circulation can impart a shearing flow at the boundaries, which can also suppress the emergence of Rayleigh-Taylor instabilities [*Richter*, 1973].

[53] By far the most important mechanisms observed in our simulations are mechanisms 3 and 4 as we have already seen in Figure 7, with some evidence for mechanisms 1 and 2. In Figure 10 we show a magnified view of the temperature field at three time steps for a mantle with Martian dimensions and a no-slip upper boundary, where the CMB is heated by hundreds of degrees K (R = 500 km, v_i = 15 km s^{-1}, $n = n_0$). In this case, two roots of preexisting plumes are pushed centerward by the return spreading flow, and coalesce. The triple-hump structure that occurs in a basal isotherm (visible at $t = t_2$) suggests that a protodiapir may have formed directly under the perturbation before merging with adjacent plumes. It is possible this was caused by the mechanisms described in items 1 and 2 above, i.e., direct heating by the perturbation, or a local buoyancy anomaly formed by the ascending motions. In the last frame ($t = t_3$) a "megaplume" has formed from the merging of plume roots with the protodiapir in the basal TBL.

5. Convection Model Perturbations II

[54] Type I perturbations exhibit a characteristic size and temperature. The characteristic temperature increase ΔT_p is given by the average difference between the geotherm and solidus. A characteristic size scale λ_p is given by the depth at which shock heating drops below ΔT_p. For the case depicted in Figure 4b, these values can be read from the abscissa and ordinate where the plotted curves intersect (e.g., $\lambda_p \approx 1100$ km and $\Delta T_p \approx 500$ K). Insofar as a thermal perturbation can be described by a characteristic magnitude and length scale, quantifiable properties of the subsequent evolution may be simple functions of dimensionless groups

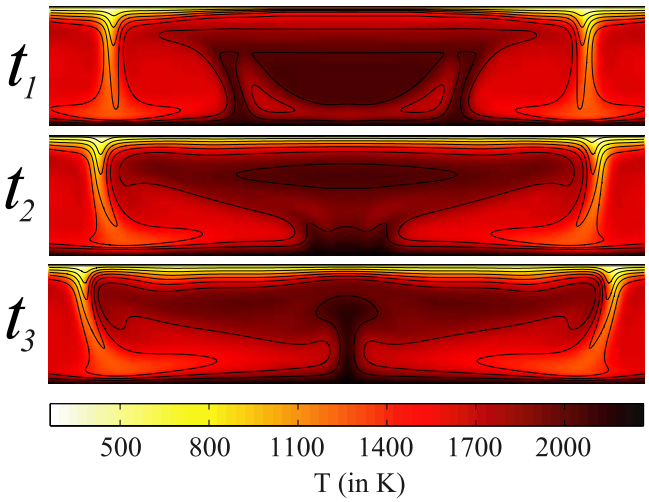

Figure 10. Evolution of the temperature field (magnified view) following the insertion of a thermal perturbation (R = 500 km, v_i = 15 km s^{-1}, $n = n_0$; $Ra = 10^5$, rigid upper boundary, Martian mantle properties). In this case the core-mantle boundary (CMB) is heated directly, and shock heating raises CMB temperatures by hundreds of degrees. The anomaly-driven circulation focuses flow in the basal TBL directly under the anomaly, causing instabilities and plumes to coalesce. A giant pulse of hot material sourced from the basal TBL occurs by $t = t_3$. The times corresponding to each frame are t_1 = 25 Ma, t_2 = 275 Ma, and t_3 = 560 Ma.

comprising these quantities. In addition to the Rayleigh number, the relevant dimensionless groups are

$$\Lambda \equiv \lambda_p/\lambda_m \tag{14}$$

$$\Theta \equiv \Delta T_p/\Delta T_c \tag{15}$$

where λ_m is the thickness of the convecting layer and ΔT_c is the temperature contrast driving mantle convection (i.e., the applied temperature contrast for 100% bottom heating, and the temperature contrast spanning a conductive geotherm in the absence of convection for the case of 100% volumetric heating).

[55] Type II perturbations are constructed by raising mantle temperatures across a semicircular region of radius λ_p by the amount ΔT_p (with no imposed solidus ceiling). At the end of section 7 we relate the parameters Θ and Λ of type II perturbations to the characteristic size and magnitude of type I perturbations resulting from impacts with a range of projectile radii and velocities, and model mantles with terrestrial and Martian properties. Note that according to our definition of type I perturbations, the corresponding value of Θ is mostly determined by the planet's thermal structure (i.e., the mean difference between solidus and geotherm, and the convective driving temperature) in the case of impacts large enough to significantly heat the lower mantle. In time-lapse movies of the temperature and velocity fields, all features of the postheating evolution described in section 4 for type I perturbations are also observed for perturbations of type II.

6. Time Scale of Spreading

[56] We turn now to quantifying the effects of impact heating for a thermal perturbation that can be described by a characteristic temperature and size (type II). Our goals in this section are to quantify properties of the qualitative description in section 4, and especially the spreading time t_s at which the spreading stage ends, for a range of conditions. Above all, we seek an expression for t_s.

6.1. Scaling Arguments

[57] As mentioned in section 5, the relevant dimensionless groups are the Rayleigh number Ra and two dimensionless numbers that characterize the magnitude and size of the perturbation, Θ and Λ, defined in equations (14) and (15). We start by posing an *ansatz* for the spreading time, as a scaling relation that comprises all of the relevant dimensionless groups:

$$t_s/t_m = f\left(\Lambda, \Theta, Ra_{(H)}\right) \tag{16}$$

$$t_s = K_0 \Theta^{\alpha} \Lambda^{\beta} Ra_{(H)}^{\gamma} \tag{17}$$

where t_m is a characteristic time scale associated with convection and K_0 is a dimensional coefficient. ($Ra_{(H)}$ represents the volumetric or bottom-heating Rayleigh number.) This general form can be motivated by considering the competition between the spreading motion of a viscous gravity current and convection in the ambient fluid. For example, a simple boundary layer theory supplies a characteristic velocity for 2-D convection in the case of 100% bottom heating and a stress-free upper boundary [*Schubert et al.*, 2001]:

$$v_{\mathrm{conv}} = (1/3)(\kappa/\lambda_m)Ra^{2/3} \tag{18}$$

where κ is thermal diffusivity and λ_m is the convecting layer thickness. Assuming that motions in the ambient fluid can be ignored, the front velocity for a viscous gravity current that spreads along a stress-free boundary in two dimensions with an ambient density contrast $\Delta\rho_p$, constant cross-sectional area λ_p^2, and viscosity μ (for the current and ambient fluid), exhibits the following scaling with time t [*Lister and Kerr*, 1989]:

$$v_{\mathrm{grav}} \sim \left(\frac{\Delta\rho_p g \lambda_p^4}{\mu}\right)^{1/3} t^{-2/3}. \tag{19}$$

To estimate the spreading time scale, we can solve for the time when these two velocities become roughly equal. Because we are considering only temperature-related density contrasts, we may set $\Theta = \Delta\rho_p/\Delta\rho_m$ where $\Delta\rho_m$ is the density contrast driving mantle convection. Setting

Table 1. Estimated Value of the Parameter ξ for the Impact Magnitude $\Upsilon \equiv \Theta\Lambda^{\xi}$ to Achieve an Optimal Collapse[a]

Set	$Ra_{(H)}/10^5$	BC	IC	Ht	ξ	68.3%	95.4%	99.7%
A	0.75	f	t.i.	b	2.1	±0.03	±0.17	±0.27
A	2.50	f	t.i.	b	2.4	±0.08	±0.13	±0.23
A	7.50	f	t.i.	b	2.8	±0.02	±0.12	±0.18
A	10.0	f	t.i.	b	2.9	±0.10	±0.11	±0.21
A	25.0	f	t.d.	b	3.0	±0.06	±0.16	±0.46
B	0.75	r	t.i.	b	2.1	±0.09	±0.19	±0.22
B	2.50	r	t.i.	b	2.5	±0.06	±0.16	±0.24
B	7.50	r	t.d.	b	3.0	±0.16	±0.36	±0.56
B	10.0	r	t.d.	b	2.6	±0.12	±0.28	±0.38
B	25.0	r	t.d.	b	2.9	±0.19	±0.58	±0.98
C	9.45	f	t.d.	v	2.0	±0.47	±0.97	±1.13
C	23.6	f	t.d.	v	3.1	±0.26	±0.66	±0.86
C	104	f	t.d.	v	4.3	±0.37	±0.94	±1.34
C	154	f	t.d.	v	3.7	±0.22	±0.42	±0.68
C	533	f	t.d.	v	2.9	±0.13	±0.27	±0.37
D	9.45	r	t.d.	v	3.7	±0.33	±0.57	±0.83
D	23.6	r	t.d.	v	2.9	±0.55	±1.25	±1.75
D	104	r	t.d.	v	3.8	±0.25	±0.45	±0.75
D	154	r	t.d.	v	3.6	±0.27	±0.37	±0.53
D	533	r	t.d.	v	4.1	±0.17	±0.27	±0.57

[a]The value of the parameter ξ is estimated by minimizing the sum of standard deviations about a running average in plots of v_{stag} versus $\Theta\Lambda^{\xi}$. Confidence limits (68.5%, 95.4%, 99.7%) were obtained from a bootstrap using $N = 1000$ random samplings with replacement. The abbreviations and labels signify the following: set identifies the calculation set; $Ra_{(H)}$ is the Rayleigh number; BC is upper boundary condition (where f is stress-free and r is rigid (i.e., no-slip)); IC is initial condition (where t.i. is time-independent and t.d. is time-dependent). Ht is heat source (where b is 100% bottom heating and v is 100% volumetric heating). Each subset (each line of the table) represents 400 calculations, and all were used to obtain estimates of ξ and the confidence limits. The unweighted average of ξ (for the entire table) is 3.02, with a standard deviation of 0.66.

$\Lambda \equiv \lambda_p/\lambda_m$, we obtain by equating (18) and (19) and solving for t

$$t_s \sim \frac{\lambda_m^2}{\kappa}\Theta^{1/2}\Lambda^2 Ra^{-1/2} \tag{20}$$

In the case where equation (19) is replaced with the appropriate scaling relation for a viscous gravity current that spreads along a rigid boundary [*Huppert*, 1982], we instead find that $\alpha = 1/4$, $\beta = 3/2$, and $\gamma = -1/2$ in equation (17), where the Rayleigh number exponent is assumed to be 3/5 in equation (18) for this case. For a stress-free upper boundary and 100% volumetric heating, $\alpha = 1/2$, $\beta = 2$, $\gamma = -1/4$. As we will see later in this section, this simple scaling analysis gives a reasonable estimate for the values of α and γ, as well as the relative magnitude and sign of all the parameters in equation (17). In what follows, we derive empirically the values of these parameters using a large set of numerical calculations.

6.2. Numerical Models and Measured Quantities

[58] As before (section 4), for each boundary condition and set of input parameters we obtained quasi steady state solutions of the governing equations (i.e., where the globally averaged velocity is unchanging or fluctuates about a stable mean). We added perturbations of type II to these temperature field solutions and then computed the subsequent evolution until $t > t_s$.

[59] Our calculations can be grouped into four sets, designated A, B, C, and D, according to upper boundary condition (no-slip or stress-free) and heat source (100% bottom or volumetric heating). Each set is made up of five subsets, one for each of five Rayleigh numbers, where these are $Ra/10^5 = \{0.75, 2.50, 7.50, 10.0, 25.0\}$ for bottom heating and $Ra_H/10^5 = \{9.45, 23.6, 104, 154, 533\}$ for volumetric heating (as summarized in Table 1). For each Rayleigh number (i.e., in each subset) we performed 400 simulations, for every combination of 20 values of Θ and Λ, for a grand total of $4 \times 5 \times 400 = 8000$ simulations. The values of Λ are $\{0.05, 0.10, 0.15.., 1.00\}$ for all subsets, and the range in Θ depends on the amount of internal heating (since this determines the convective driving temperature ΔT_c). Among the cases with bottom heating, many of the initial conditions (the starting solutions) are time-independent (see Table 1). See section 4 for additional details regarding mesh dimensions and boundary conditions. Perturbations were emplaced between downwellings and plumes, i.e., centered on rolls.

[60] At regular time intervals, we recorded the temperature and velocity at each row of nodes, averaged across the entire mantle width, as well as over one quarter of the width, centered on the perturbation ("quarter frame"). A time series of the mantle velocity v averaged over the quarter frame is shown in the top of Figure 11 for one of the smallest and weakest perturbations, in a calculation belonging to set A ($Ra/10^5 = 7.5$, 100% bottom heating, stress-free upper B.C.). In the case of time-independent initial conditions like this one, even a weak perturbation has a noticeable effect. In this case, the mean flow velocity is not initially accelerated above the starting value of 7 mm a^{-1}.

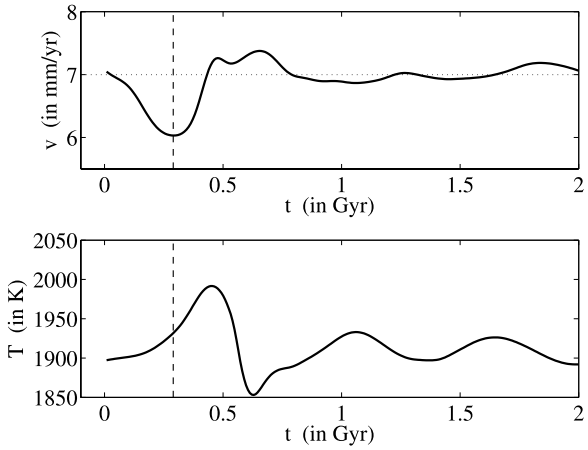

Figure 11. (Top) Plot of mean flow velocity for one quarter slice of the mantle (centered on the perturbation), where the minimum value indicates the stagnation time t_{stag}, marked with a dashed line ($Ra = 7.5 \times 10^5$, stress-free upper boundary, 100% bottom heating, $\Lambda = 0.25$, $\Theta = 0.11$). Although the perturbation in this case was small and low-temperature, its effects are noticeable in this initially time-independent solution. (Bottom) For the same calculation, a plot of mean temperature of nodes at a fixed depth inside the basal TBL. Steadily increasing or decreasing temperature indicates a steadily thickening or thinning basal TBL, respectively. The global maximum indicates t_b, the time until maximum size and draining of the basal TBL, which is normally $\approx 1.5 t_{\text{stag}}$.

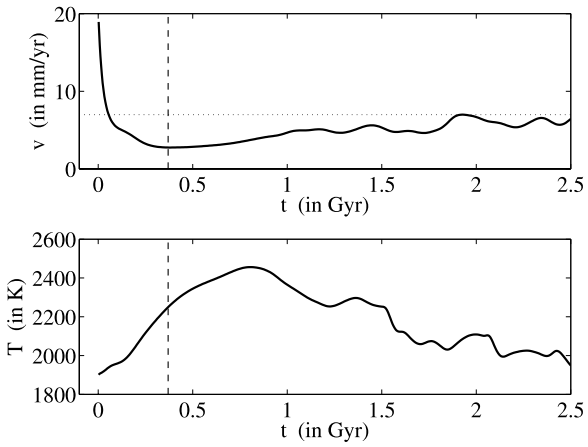

Figure 12. The same quantities as plotted in Figure 11 from an identical starting condition, although with a stronger perturbation (Λ = 0.50, Θ = 0.59). The quarter-frame averaged velocity is initially accelerated well above the preperturbation value of 7 mm a^{-1} (dotted line) and drops to less than half this value at the stagnation time (dashed line).

Instead it drops to a minimum value which determines the "stagnation time," t_{stag} (dashed line). Movies of the temperature field for this case reveal that the perturbation hardly flattens or spreads at all (except by diffusion). Instead, the anomaly drifts into the nearest downwelling and is drained into it. The minimum velocity in the time series of Figure 11 occurs when the perturbation reaches the fastest portion of the downflow (i.e., when it interferes with the fastest region of the convective flow field, at roughly 1/2 the mantle depth). Throughout the remainder of this report, "stagnation" refers to flow in the layer (or a portion of it) reaching a minimum averaged velocity, and does not mean that flow has halted. As we saw in section 4, larger perturbations can create large zones that are virtually stagnant, and the name derives from this observation.

[61] While the flow slows, the basal TBL thickens, and is drained shortly afterward at time t_b. This lapse ($t_b - t_{stag}$) is illustrated in the time series at the bottom of Figure 11, which shows the temperature at a fixed depth within the basal TBL. As the TBL thickens, this temperature increases, and decreases when the layer is drained while instabilities grow and detach, or become swept into adjacent plumes.

[62] The corresponding time series are shown in Figure 12 for the same convection model and starting condition although with a stronger perturbation, where Λ = 0.5 and Θ = 0.59. In this case, the quarter-frame averaged velocity is accelerated to nearly three times its preperturbation value (v_0) and plummets during the short-lived flattening stage. The temporal minimum of velocity averaged over a quarter slice of the mantle is less than half of v_0. The thickening and draining of the basal TBL is readily noticeable in the corresponding time series for temperature at a fixed depth in this layer (Figure 12, bottom). By recording the times of the velocity minimum (t_{stag}) and temperature maximum (t_b) in these time series for all calculations, we find that a value $t_b/t_{stag} \approx 1.5$ occurs with the greatest frequency.

[63] We have estimated the spreading time t_s indirectly, by measuring two time scales which are coupled to the spreading time for a range of conditions. These are the stagnation time, t_{stag}, and the "leveling time," t_{lev}. This correspondence was noted in time-lapse movies of the temperature field, generated for a subset of all calculations. The stagnation time is reached when the mean mantle velocity in the quarter frame (one quarter slice of the mantle centered on the perturbation), averaged over long time intervals, reaches its minimum value. This occurs after spreading has ceased, and remnants of the perturbation sink into nearby downwellings, causing the fastest regions of the velocity field to slow down. For a range of conditions, the spreading time scale is therefore approximately equal to the stagnation time scale minus the time required for perturbation remnants to sink into nearby downwellings, t_{sink}. This latter time is a function of the Rayleigh number only. Defining t_{s1} to be an estimate of the spreading time t_s derived from the stagnation time scale, we can write

$$t_{stag} = t_{sink} + t_{s1} \Longrightarrow t_{s1} = t_{stag} - g_1\left(Ra_{(H)}\right) \tag{21}$$

where g_1 is some function of $Ra_{(H)}$.

[64] For each calculation we have stored at regular time intervals the horizontal temperature profile at the base of the preimpact upper TBL. The quantity σ_T is the standard deviation of this domain-spanning temperature profile. The "leveling time scale" t_{lev} is defined as the time when σ_T reaches its minimum value. This corresponds to a time when the spreading flow has slowed or halted, so that no additional downwellings are destroyed or fused (which causes σ_T to decrease) and before new ones emerge (which causes σ_T to increase). Therefore, for a range of conditions, t_{lev} approximately corresponds to the end of spreading. The leveling time is offset from the spreading time estimate t_{s2}

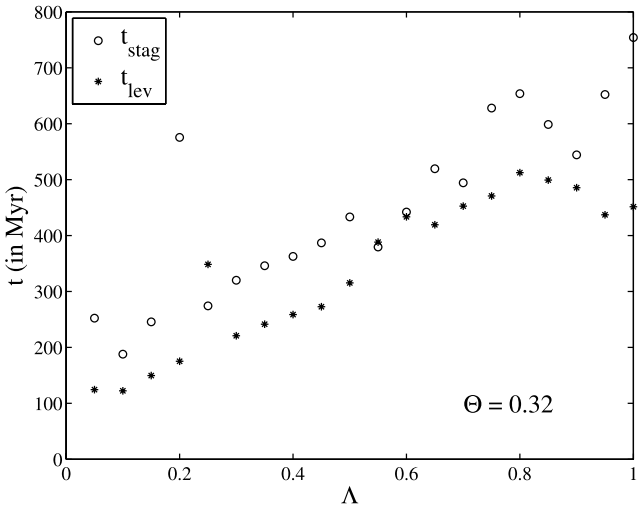

Figure 13. Stagnation and leveling time scales (t_{stag} and t_{lev}, respectively) versus dimensionless perturbation size Λ, for dimensionless perturbation temperature Θ = 0.32 (Set A; $Ra = 10^6$, stress-free upper boundary, 100% bottom heating). Both are approximately linear functions of Λ up to Λ = 0.8, where the spreading anomaly reaches a global extent. Subtracting the y axis intercepts, both quantities are estimates of the spreading time (t_{s1} and t_{s2}, respectively).

Table 2. Estimated Parameter Values for Expressions Relating the Stagnation and Leveling Time Scales to Perturbation Size, Perturbation Temperature, and Rayleigh Number[a]

Set ID:t	$Ra_{(H)}/10^5$	BC	IC	Ht	$K_1/10^5$	ζ	η
A:t_{stag}	[0.75, 10]	f	t.i.	b	5.33	0.00	−0.59
B:t_{stag}	[0.75, 2.5]	r	t.i.	b	1.97	0.00	−0.44
A:t_{lev}	[0.75, 10]	f	t.i.	b	1.29	0.40	−0.50
B:t_{lev}	[0.75, 7.5]	r	t.i.	b	0.331	0.00	−0.31
C:t_{lev}	[100, 530]	f	t.d.	v	1810	0.00	−0.99

[a]In general, $\{t_{\mathrm{stag}}, t_{\mathrm{lev}}\} = f(\Theta, \Lambda, Ra_{(H)})$, where f is a nontrivial function of these variables. For a range of conditions, $\{t_{\mathrm{stag}}, t_{\mathrm{lev}}\} \approx \{t_{s1}, t_{s2}\} + K_1\Theta^{\zeta}Ra_{(H)}^{\eta}$, where the relation for spreading time scale has the form $\{t_{s1}, t_{s2}\} = K_0\Theta^{\alpha}\Lambda^{\beta}Ra_{(H)}^{\gamma}$ (see Table 1). Estimates of ζ and η are supplied in the table for t_{stag} and t_{lev} in sets A–C. Only in the case of set A and the quantity t_{lev} is ζ nonzero. In this case, $\zeta = 0.40$ (68.3% confidence limit: ±0.07; 95.4% confidence limit: ±0.17), and $\eta = -0.50$ (68.3% confidence limit: ±0.06; 95.4% confidence limit: ±0.10). Confidence limits were obtained from a bootstrap using $N = 1000$ random samplings with replacement. Since these correspond to the values of α and γ, respectively, $t_{\mathrm{lev}} \approx (K_0\Lambda^{\alpha} + K_1)\Theta^{\beta}Ra_{(H)}^{\gamma}$ for this case only. The abbreviations and labels signify the following: set ID: t identifies the calculation set and the time scale; $Ra_{(H)}$ is range in Rayleigh numbers; BC is upper boundary condition (where f is stress-free and r is rigid (i.e., no-slip)); IC is initial condition (where t.i. is time-independent and t.d. is time-dependent); Ht is heat source (where b is 100% bottom heating and v is 100% volumetric heating).

by a quantity that depends on $Ra_{(H)}$ in the case of sets B and C, and Ra in addition to Θ in the case of set A:

$$t_{s2} = t_{\mathrm{lev}} - g_2\left(\Theta, Ra_{(H)}\right) \tag{22}$$

Figure 13 depicts the approximately linear trend of both time scales as a function of Λ for a subset of calculations in set A (i.e., stress-free upper boundary, 100% bottom heating, and $Ra = 10^6$, $\Theta = 0.32$). The functions g_1 and g_2 in equations (21) and (22) were estimated by fitting a line to plots of t_{lev} and t_{stag} versus Λ to obtain the intercept values. These results are supplied in Table 2.

[65] We have said that equations (21) and (22) are valid for a range of conditions, and we turn now to describing these. These conditions have been determined from close examination of movies generated for the evolution of the temperature and velocity fields for a subset of the calculations in each of the sets A, B, and C.

[66] The rollover in t_{lev} that occurs at $\Lambda = 0.8$ in Figure 13 is a common feature of such curves. This corresponds to a configuration of the temperature field in which nearly all downwellings have been swept together or destroyed. Larger perturbation sizes only cause the system to achieve this configuration sooner; that is, t_{lev} decreases with larger Λ. In the case of large Θ, this corresponds to the spreading flow reaching a global extent. This feature of t_{lev} is therefore a consequence of the system's finite size.

[67] Rollovers and plateaus of this sort also occur in plots of t_{stag} versus Λ, at values of Λ above which the perturbation destroys nearby downwellings, causing the flow in this region (the quarter slice centered on the perturbation) virtually to stagnate. In these cases, the quarter-sample averaged velocity is not sensitive to (decouples from) the large-scale spreading flow, so that t_{stag} does not reflect t_s.

[68] It should be noted also that t_{s1} and t_{s2} are estimates of the time when the spreading flow is slowed and then halted by downwellings on one of the two spreading fronts (e.g., see frames t_3 through t_5 in Figure 7: leftward spreading

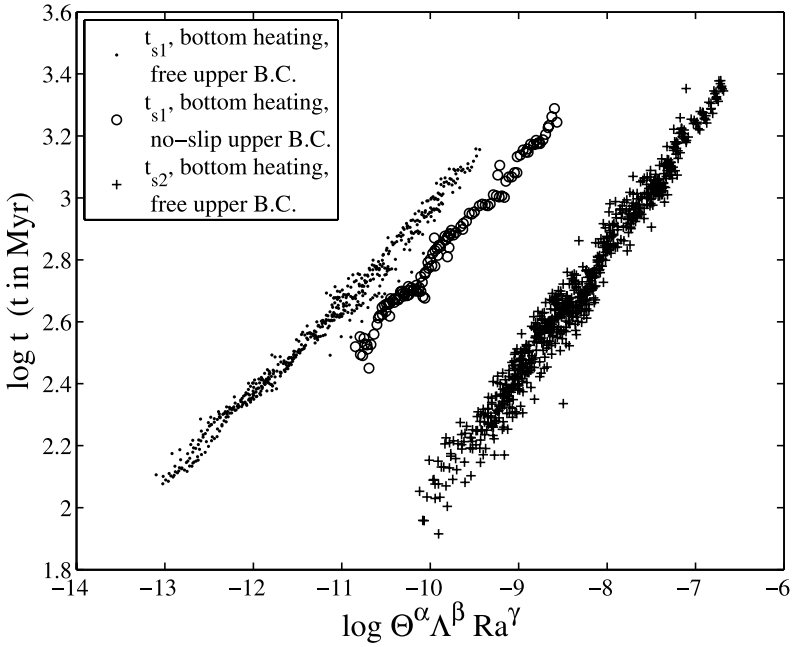

Figure 14. Spreading time scales t_{s1} and t_{s2} plotted as a function of $\Theta^{\alpha}\Lambda^{\beta}Ra^{\gamma}$, where the exponents have been estimated using a simple parameter search, minimizing the norm of residuals from a least squares linear regression in log-log space. Note that each data cloud corresponds to a different set of estimated parameter values (for α, β, and γ) where these are listed in Table 1 along with 95.4% confidence limits and the range in Rayleigh number. Points below the crossover limit were excluded (see text for discussion).

Table 3. Estimated Parameter Values for Spreading Time Scale Relations, $\{t_{s1}, t_{s2}\} = K_0\Theta^{\alpha}\Lambda^{\beta}Ra^{\gamma}$

Set ID:t	$Ra_{(H)}/10^5$	BC	IC	Ht	c.c.	n	$K_0/10^5$	α	β	γ
A:t_{s1}	[0.75, 10]	f	t.i.	b	N	767	6.97	0.30 ± 0.03	0.92 ± 0.02	−0.50 ± 0.01
A:t_{s1}	[0.75, 10]	f	t.i.	b	Y	552	6.97	0.29 ± 0.02	1.01 ± 0.02	−0.49 ± 0.01
B:t_{s1}	[0.75, 2.5]	r	t.i.	b	N	185	12.2	0.42 ± 0.09	1.07 ± 0.04	−0.50 ± 0.03
B:t_{s1}	[0.75, 2.5]	r	t.i.	b	Y	119	9.84	0.33 ± 0.06	1.03 ± 0.06	−0.53 ± 0.02
A:t_{s2}	[0.75, 10]	f	t.i.	b	N	911	10.4	0.37±0.02	1.07 ± 0.05	−0.51 ± 0.02
A:t_{s2}	[0.75, 10]	f	t.i.	b	Y	747	10.3	0.40 ± 0.03	0.96 ± 0.03	−0.52 ± 0.01
B:t_{s2}	[0.75, 7.5]	r	t.i.	b	N	418	12.5	0.65 ± 0.06	1.05 ± 0.05	−0.48 ± 0.02
B:t_{s2}	[0.75, 7.5]	r	t.i.	b	Y	381	14.4	0.62 ± 0.05	0.96 ± 0.04	−0.50 ± 0.02
C:t_{s2}	[104, 533]	f	t.d.	v	N	309	0.147	0.30 ± 0.03	1.03 ± 0.04	−0.13 ± 0.04

[a]Parameter values were estimated by means of a simple parameter search, minimizing the norm of residuals from a least squares linear regression in log-log space. Also given are 95.4% confidence limits obtained from a bootstrap (N = 1000 random samplings with replacement), where set ID: t identifies the calculation set and the time scale; $Ra_{(H)}$ is the range in Rayleigh numbers; BC is the upper boundary condition (where f is stress-free and r is rigid (i.e., no-slip)); IC is the initial condition (where t.i. is time-independent and t.d. is time-dependent); Ht is the heat source (where b is 100% bottom heating and v is 100% volumetric heating); c.c. indicates whether a threshold was applied to remove perturbations below the crossover transition; n indicates the number of simulations used in the inversion (i.e., number of model results for a given perturbation size and temperature). Estimated parameter values for individual subsets (for individual Rayleigh numbers) are supplied in Tables 3 and 4 of the auxiliary material, along with the crossover condition for each case.

current). In those cases where the spreading flow is greatly slowed by a downwelling that is ultimately breached (i.e., severed and bypassed), the spreading time can greatly exceed the trend shown in Figure 13. Examples of these obvious outliers are represented by the points $\Lambda = 0.2$ and $\Lambda = 0.25$. For this reason, t_{s1} and t_{s2} should be considered to represent a lower bound for the absolute spreading time scale t_s.

[69] Finally, there are numerous cases for which either t_{stag} or t_{lev} (or both) are completely decoupled from the spreading time scale, for most or all perturbation magnitudes. This is often the case for time-dependent initial conditions, where the spontaneous emergence and disappearance of downwellings, near and far away from the spreading region, plays a large role in determining t_{stag} and t_{lev}. For example, none of the calculations in set D (100% volumetric heating with a no-slip upper boundary) could be used for this part of the analysis. The stagnation time was only coupled to the spreading time for the initially time-independent solutions in the case of 100% bottom heating. Significantly, however, the leveling time scale was strongly coupled to the spreading time scale for three Rayleigh numbers in set C, all with strongly time-dependent initial conditions (100% volumetric heating, stress-free upper boundary).

6.3. Estimated Parameter Values

[70] We have estimated the values of the exponents in equation (17) for t_{s1} and t_{s2} by means of a simple parameter search, minimizing the norm of residuals from a least squares linear regression in log-log space. Only those calculations satisfying the aforementioned conditions were used in the inversion. For each set of calculations (A, B, and C), the inversion was first performed for each Rayleigh number separately. This revealed a significant crossover transition from a distinct behavior at very small perturbation magnitudes. We performed the inversion twice for each Rayleigh number, in one case keeping and in the other excluding perturbation magnitudes below the crossover transition. The inversion was also performed for calculations derived from each set as a whole (multiple Rayleigh numbers), as shown in Figure 14 for calculations in sets A and B. The estimated exponent values for this global inversion are supplied in Table 3. We have reported also the 95.4% confidence limits obtained from a bootstrap analysis, using N = 1000 random samplings with replacement [*Press et al.*, 1988]. The results from the inversions performed separately for each Rayleigh number are printed in Tables 3 and 4 of the auxiliary material along with the crossover transition for each case. There was no crossover transition noted for t_{s2} in set C, and therefore no threshold was applied.

[71] According to the results in Table 3, estimates of α, β, and γ for t_{s1} are essentially identical for free and rigid upper boundaries in the case of bottom heating ($\alpha \approx 0.3$, $\beta \approx 1.0$, $\gamma \approx -0.5$), where the crossover threshold has been applied. For the case of t_{s2}, the estimates of β concur for both boundary conditions and for bottom as well as volumetric heating ($\beta \approx 1.0$). The estimates of γ (for t_{s1} and t_{s2}) agree for the case of bottom heating, and are very different (as expected) for volumetric heating. The most significant difference occurs in the estimates of α for t_{s2}. In particular, α is larger than corresponding estimates for t_{s1}, and its value for the case of a no-slip upper boundary (α = 0.62) is significantly greater than its value for the case of a stress-free upper boundary (α = 0.40). Finally, note that the estimated values of α and β for t_{s2} in set C (free upper boundary, 100% volumetric heating) are essentially indistinguishable from the estimates of α and β for t_{s1} in set A (free upper boundary, 100% bottom heating).

[72] In summary, the results in Table 3 suggest that $\beta \approx 1$ for both boundary conditions and heat sources, $\gamma \approx -0.5$ for bottom heating (both boundary conditions) and $\gamma \approx -0.13$ for volumetric heating and a free upper boundary. Estimates of the exponent α range from 0.3 to 0.4 for the case of a stress-free upper boundary, and from 0.33 to 0.62 for the case of a rigid upper boundary. It is worth noting that the simple estimates obtained by deriving equation (20) were not far from the mark in the case of α and γ, and predicted correctly that $\beta > \alpha > \gamma$.

7. Global Stagnation Criterion

[73] We turn now to finding those values of Θ and Λ which guarantee that a perturbation reorganizes the circulation in model mantles at a global scale. As already mentioned, one of the most significant consequences of the perturbation-driven flow is that mantle velocities are greatly depressed. To begin, we define the "stagnation

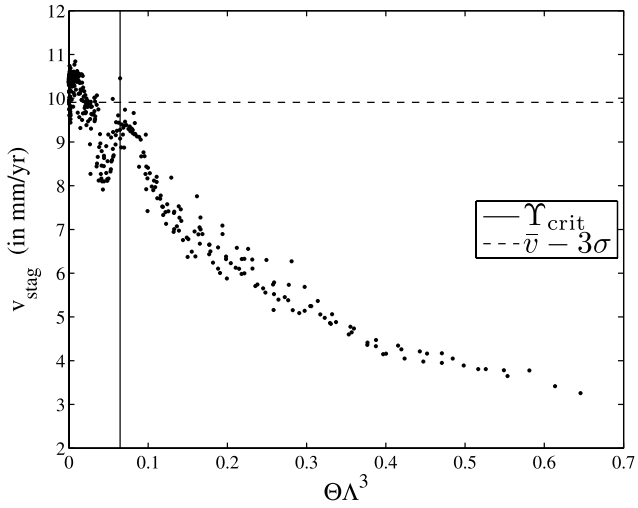

Figure 15. Stagnation velocity v_{stag} (i.e., temporal minimum of the globally averaged velocity following anomaly insertion) versus perturbation magnitude $\Upsilon = \Theta\Lambda^3$ for $Ra = 2.5 \times 10^6$ in the case of 100% bottom heating and a stress-free upper boundary (N.B., a time-dependent initial condition). The critical perturbation magnitude (Υ_{crit}) corresponds to that value of $\Theta\Lambda^3$ above which all perturbations depress the globally averaged mantle velocity to 3σ below its mean value.

velocity" v_{stag} as the minimum (in time) of the globally averaged mantle velocity. We find that v_{stag} is a nontrivial function of the quantity $\Theta\Lambda^{\xi}$, which therefore provides a convenient measure of the perturbation magnitude in terms of its effect on the mantle as a whole. The value of the exponent ξ was estimated by means of a simple parameter search, minimizing the sum of standard deviations about a running average of v_{stag} in order of increasing $\Theta\Lambda^{\xi}$. The estimated values of ξ are reported in Table 1, along with confidence limits derived from a bootstrap analysis. It is worth noting a possible trend in ξ with increasing Rayleigh number, although an exact relationship is hard to establish on the basis of these results. The mean value of ξ, when averaging over all subsets in Table 1, is 3.02. In what follows, the "perturbation magnitude" refers to the quantity $\Upsilon \equiv \Theta\Lambda^3$.

[74] We define "global stagnation" as an event in which the globally averaged mantle flow velocity is depressed three standard deviations below its temporal mean, $\bar{v}$; that is, $v < \bar{v} - 3\sigma_v$ where σ_v is the temporal standard deviation about $\bar{v}$ prior to insertion of the anomaly. The critical perturbation magnitude Υ_{crit} is that value of Υ above which all perturbations cause global stagnation. Figure 15 shows v_{stag} as a function of the perturbation magnitude for the case of 100% bottom heating, a stress-free upper boundary, and $Ra = 2.5 \times 10^6$ (a time-dependent initial condition). The value of $\bar{v} - 3\sigma_v$ has been labeled, along with Υ_{crit}. First, it is worth noting that this curve has a nontrivial shape. The shape of $v_{stag} = f(\Upsilon)$ is different for each set in Table 1, often differing among subsets (i.e., different Rayleigh numbers). Second, it should be emphasized that while global stagna-

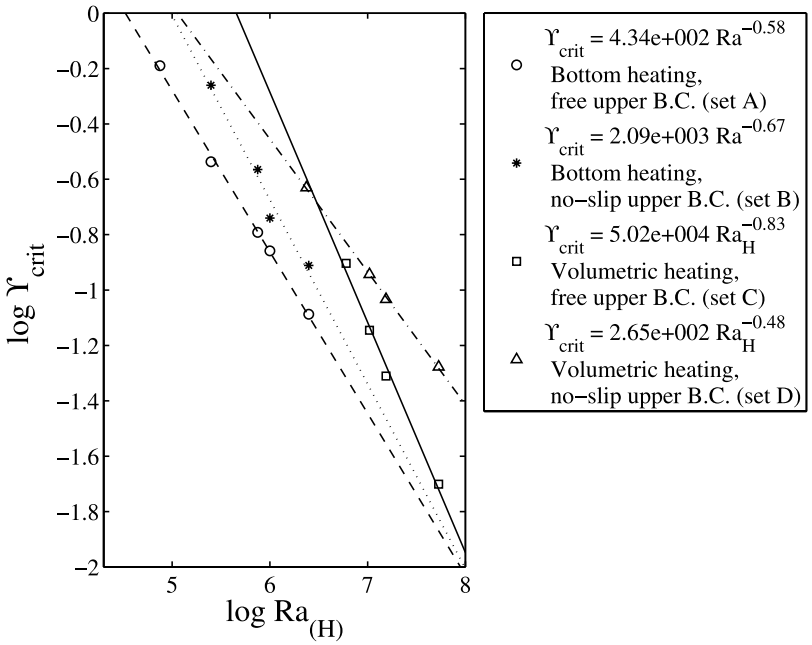

Figure 16. Critical perturbation magnitude Υ_{crit} versus Rayleigh number and linear fits used to obtain the global stagnation criterion for the following conditions: 100% bottom heating with free and no-slip upper boundaries; 100% volumetric heating with free and no-slip upper boundaries. Note that an internal-heating Rayleigh number is used for the latter two cases. For all values of the perturbation magnitude $\Upsilon \equiv \Theta\Lambda^3 > \Upsilon_{crit}$, the globally averaged mantle flow velocity is depressed 3σ below its temporal mean prior to anomaly insertion, $\bar{v}$. Note that not all subsets in Table 3 were used; for some of the low Ra subsets, $\bar{v} - 3\sigma_v$ was not reached for any of the impact magnitudes considered.

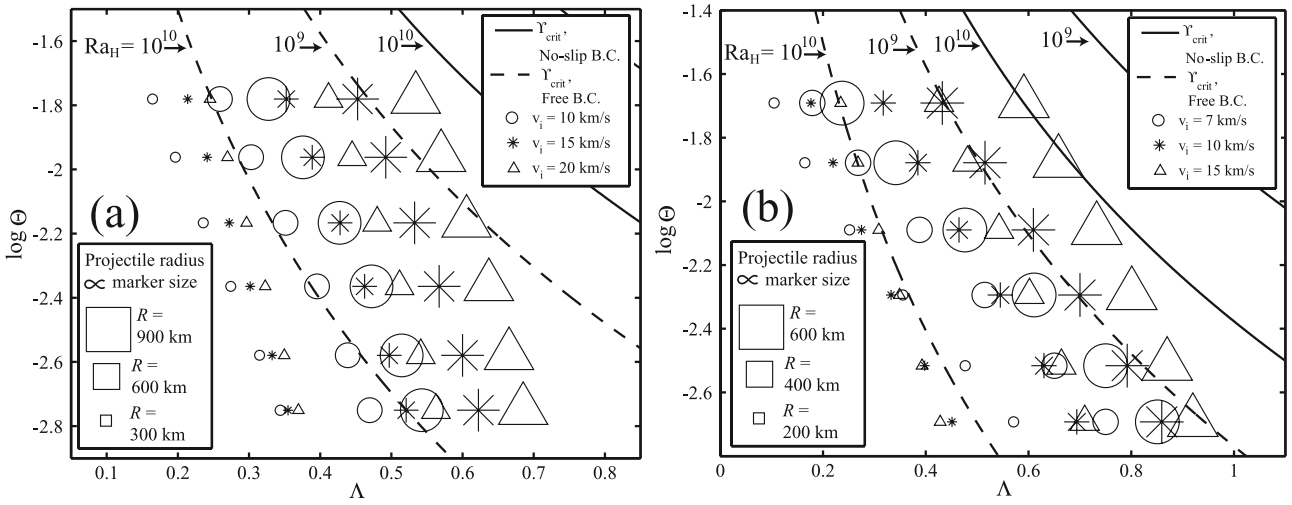

Figure 17. Diagrams relating perturbations of type I to perturbations of type II and the global stagnation criterion, $\Upsilon \equiv \Theta\Lambda^3 > \Upsilon_{crit}$ for internal-heating Rayleigh numbers 10^9 and 10^{10} in the case of a rigid (solid lines) and stress-free upper boundary (dashed lines), for a model mantle with (a) terrestrial and (b) Martian dimensions and material properties (i.e., used to calculate shock heating). In each case we have chosen an effective driving temperature ΔT_c appropriate for the early solar system (i.e., the temperature contrast spanning a conductive geotherm in the absence of convection for 100% volumetric heating; see text for discussion). In the case of Earth, $\Delta T_c = 5.5 \times 10^4$ K; and in the case of Mars, $\Delta T_c = 4.2 \times 10^4$ K. Each point represents a projectile radius, R, and incident velocity, v_i, which can be related to the dimensionless perturbation temperature and size, Θ, and Λ, respectively (where the peak shock pressure decays with exponent $n = n_0$ and the "climbing shock" method was used to calculate the amount of heating). Points that lie above a given solid or dashed curve satisfy the global stagnation criterion for the corresponding Rayleigh number and upper boundary condition and therefore will depress the globally averaged mantle flow velocity to 3σ below its temporal mean value prior to anomaly insertion. The perturbation temperature, which represents the separation between geotherm and solidus is, from top to bottom, $\Delta T_p = \{1000, 650, 400, 250, 150, 100\}$ K (where $\Theta = \Delta T_p/\Delta T_c$). Note that Λ corresponds to the dimensionless mantle depth at which the shock-heating curve crosses the solidus. See text for a discussion of values assumed for other mantle properties and section 8 in the auxiliary material for the same diagrams with different values assumed for ΔT_c.

tion occurs in many calculations for which $\Upsilon < \Upsilon_{crit}$, this quantity ($\Upsilon_{crit}$) has been defined as the perturbation magnitude above which all perturbations cause global stagnation. In this way, the condition guarantees that global stagnation is a direct consequence of the spreading flow, and not of an interaction between the spreading flow and a fortuitous configuration of the preexisting convection pattern. Note that for those subsets with a time-independent initial condition, the measured value of σ_v is vanishingly small. For those cases, we set $\sigma_v \equiv 0.12\bar{v}$, which is typically observed for time-dependent solutions.

[75] In Figure 16 we show the dependence of Υ_{crit} upon the Rayleigh number, where the explicit relation is supplied in the box at right for each of the sets A, B, C, and D. For all cases, we find that $\Upsilon_{crit} = f(Ra)$ has the form $\Upsilon_{crit} = C_0 Ra^{-q}$, where $0 < q < 1$. Significantly, the critical perturbation magnitude decreases as an inverse power law of the Rayleigh number. As the Rayleigh number increases, the perturbation magnitude required for global stagnation decreases most rapidly for volumetric heating and a stress-free upper boundary ($\Upsilon_{crit} \sim Ra^{-0.83}$) and most gradually for volumetric heating and a no-slip upper boundary ($\Upsilon_{crit} \sim Ra^{-0.48}$). It should be remembered, however, that Ra and Θ are not independent, since $Ra \sim \Delta T_c$ and $\Theta \equiv \Delta T_p/\Delta T_c$. For a given dimensionless perturbation size Λ, the critical perturbation temperature $(\Delta T_p)_{crit}$ therefore scales with Ra as $(\Delta T_p)_{crit} \sim Ra^{1-q}$.

[76] Figure 17 can be used to relate perturbations of type I to perturbations of type II and the critical perturbation magnitude, Υ_{crit}, assuming that the relations in Figure 16 are valid for (can be extended to) the large internal-heating Rayleigh numbers of early terrestrial mantles (10^9 to 10^{10}). We have plotted Υ_{crit} for 100% volumetric heating, for both free and no-slip upper boundaries. Each point represents a different projectile radius R and vertical incident velocity v_i indicated by the marker symbol and size. These can be translated to corresponding values of Θ and Λ, and compared with Υ_{crit}. Points lying above the curves of constant Υ_{crit} represent perturbations that would cause global stagnation for model mantles with terrestrial and Martian properties (e.g., shock EOS, mantle thickness with respect to depth of impact heating, and convective driving temperature).

[77] For both cases we have chosen a convective driving temperature ΔT_c appropriate for the early solar system. The convective driving temperature for the case of volumetric heating (the temperature contrast spanning a conductive profile in the absence of convection) is given by $\Delta T_c = \rho H \lambda_m^2/2k$, where ρ is a characteristic density, H is the internal heating, λ_m is the mantle thickness, and k is thermal conductivity. For the Earth we have assumed $\rho = 4{,}000$ kg m^{-3},

λ_m = 2,870 km, and k = 10 W K m^{-1}. (The value of thermal conductivity in the Earth's lower mantle is a matter of controversy; the value we have chosen lies at the middle of the range of reported estimates [*Schubert et al.*, 2001].) For the case of Mars we have assumed ρ = 3,400 kg m^{-3}, λ_m = 1,700 km, and k = 4 W K m^{-1} [*Schubert and Spohn*, 1990; *Yoder et al.*, 2003]. The value of H depends on the density of radiogenic heat production in the mantle. We assume the same value for Earth and Mars, on the basis of a modern estimate for the terrestrial mantle projected backward in time using known decay constants, as commonly used in thermal history models:

$$H = \frac{1}{\rho}\left(1.7 \times 10^{-7}\ \mathrm{Wm^{-3}}\right) \exp\left(-1.38 \times 10^{-17} t\right) \qquad (23)$$

where t is the time since planet formation in seconds [*Stevenson et al.*, 1983; *Schubert et al.*, 2001]. Assuming a time that corresponds to the Late Heavy Bombardment (~500 Ma), we obtain $\Delta T_c = 5.5 \times 10^4$ K for the Earth and $\Delta T_c = 4.2 \times 10^4$ K for Mars. We have reproduced the plots in Figure 17 for modern and intermediate values of the driving temperature in Figures S23 and S24 of section 8 in the auxiliary material.

[78] Finally, the perturbation temperature ΔT_p, which represents the separation between geotherm and solidus, is plotted in Figure 17 for ΔT_p = {1000, 650, 400, 250, 150, 100} K (from top to bottom). It should be remembered that higher Rayleigh numbers imply a hotter mantle, so that geotherms approach the solidus, limiting the size of ΔT_p and therefore of $\Theta \equiv \Delta T_p / \Delta T_c$. As Figure 17 shows for the terrestrial case, global stagnation in model mantles can be expected for $R \geq 600$ km at incident velocities in the range 15–20 km s^{-1} only for the extremely high internal heating Rayleigh number $Ra_H = 10^{10}$ and a stress-free upper boundary. For the Martian case, projectiles with $R \geq$ 600 km and incident velocity $v_i \geq 7$ km s^{-1} will cause global stagnation for $Ra_H = 10^{10}$ and a stress-free upper boundary; $v_i \geq 15$ km s^{-1} and the same radius assures the condition is met for $Ra_H = 10^9$. Perturbations in the range considered are not guaranteed to cause global stagnation for either model if the upper boundary is rigid (no-slip).

8. Alternative Convection Models

[79] Convection models with temperature-dependent viscosity are likely to respond in different ways to thermal perturbations, where this will depend heavily on the resulting viscosity contrasts. As mentioned, the time scale of viscous relaxation in the flattening stage is controlled by the ambient viscosity (outside of the perturbation) and the anomalous buoyancy of the perturbation itself, so that temperature-dependent viscosity is unlikely to have a significant effect in this stage. *Monteux et al.* [2007] found that the time and length scaling for viscous drop spreading in the transition from the advective to the diffusive regime is mostly unchanged by a strongly temperature-dependent viscosity. Nonetheless, because the interaction with downwellings is what mostly controls the duration of the spreading stage in our models, significant changes to their mechanical properties will likely affect the nature of this interaction and therefore also the spatial and temporal extent of the perturbation-driven flow.

[80] In general, convection models with a small viscosity contrast (a maximum/minimum viscosity ratio of less than 100) will resemble the isoviscous case, since the mechanical properties of the thermal boundary layer are similar to those of the mantle as a whole [*Solomatov*, 1995]. For higher viscosity ratios, convection is largely controlled by the sluggish motions of a thick and highly viscous upper boundary layer [*Solomatov*, 1995]. Thick and slow-moving downflows firmly rooted in the sluggish lid may halt the motions of the low-viscosity spreading current upon collision. Alternatively, foundering slabs that are sufficiently thin may be weakened by the high temperatures of the anomaly and severed by the spreading motion.

[81] For thick stagnant lids, all but very large perturbations will reside mostly in the immobile upper boundary layer, and will have essentially no dynamical consequence for convection in the mantle. Nonetheless, convection in the approximately isothermal regions beneath a stagnant lid and between broadly spaced sluggish downflows may respond to the largest thermal anomalies in a way that is similar to what occurs in our simulations. Since the convective driving temperature is largely determined by the overall viscosity contrast, this quantity will be significantly smaller than what has been assumed in our isoviscous models. Insofar as plumes control the location of magmatic centers in a stagnant lid mantle, the most significant consequence of the perturbation-driven flow might be the tendency for plumes to become concentrated near the center of the spreading region.

[82] Our simulations were conducted using a two-dimensional geometry, and the dynamics in three dimensions are likely to be different in important respects. The tendency of a vertical shearing flow to suppress Rayleigh-Taylor instabilities at the upper and lower boundary layers will have the greatest effect upon convective motions that are transverse to this flow [*Richter*, 1973], i.e., transverse to radial spreading. Time and length scaling with respect to perturbation magnitude will change because the flattening and spreading of the perturbation reaches a smaller spatiotemporal extent as its volume is spread out (and driving buoyancy exhausted) over three dimensions rather than two. In 3-D, upward flows in high-*Ra* convection assume a wide range of shapes depending on the amount of internal heating, from cylindrical plumes to diffuse and broad-scale upwellings. The scale of spreading may be limited less by three-dimensional structures, e.g., plumes in 2-D can significantly erode and even "behead" the spreading front, while a three-dimensional spreading flow can partially circumvent these structures. Downwellings are barriers to lateral flow in two dimensions, whereas in 3-D only very long sheet-like downflows will retard the motion completely in one of multiple directions.

[83] Going forward, this work can be extended in several ways. As mentioned, it is worthwhile repeating this exercise for more realistic temperature- and stress-dependent rheologies and geometries in order to obtain the scaling in these cases for the spreading time and global stagnation criterion. In addition to the important differences mentioned above, since the growth rate of protodiapirs depends inversely upon the ambient viscosity, the effects of direct heating of the CMB will be more pronounced, since even temperature changes of hundreds of degrees will modify mantle viscos-

ities above the basal TBL by orders of magnitude. It will be important also to use realistic estimates of the buoyancy associated with retained melts in the shock-heated volume. For this purpose, the same experiments can be conducted with perturbations having a material instead of thermal buoyancy.

9. Geological Implications

[84] Owing to significant simplifications in our models, as well as our limited knowledge of the thermal state and structure of young planetary interiors, it is not possible to draw firm conclusions from our work regarding the evolution of early terrestrial mantles, or to apply directly the scaling relationships obtained above. Nonetheless, some of the processes that occur in our simulations may have played an important role in the early solar system, and we turn now to consider these in the context of early Mars as a way of highlighting significant questions for further study.

[85] Recent work has demonstrated the plausibility of a giant impact origin for the crustal dichotomy [*Marinova et al.*, 2008; *Nimmo et al.*, 2008]. *Andrews-Hanna et al.* [2008] extended the dichotomy boundary beneath Tharsis, completing the circumference of an immense, elliptical impact basin. Mars' internal magnetic field possibly survived dichotomy formation, since small magnetic anomalies occur in the northern lowlands that were not erased by subsequent magmatism [*Acuña et al.*, 1999]. If mantle convection had not already reached the highly sluggish or stagnant lid regime by the time of the dichotomy-forming impact, then the resulting buoyancy perturbation might have had profound consequences for convection in the mantle. Assuming that the "stagnation" effect illustrated in our models occurs also in three-dimensional spreading flows for relevant rheologies, this current might well have suppressed convection throughout portions of the Martian mantle. Processes which tend to diminish the efficiency of mantle convection prevent efficient cooling of the core-mantle boundary and therefore tend to suppress convection in the outer core as well [*Stevenson*, 2001]. The spreading stage that followed a Borealis impact (and possibly subsequent large impacts) might have hastened the extinction of the Martian dynamo and internal magnetic field. This mechanism would not permanently suppress the dynamo, however, since mantle convection resumes when the spreading stage has ended. A significant interruption of convection in the mantle, depending on the time scale of its duration, is an important consideration for thermal history models as well.

[86] It is not known when Tharsis volcanism began, but many lines of evidence suggest that a significant proportion of this immense crustal load was in place by the late Noachian [*Banerdt and Golombek*, 2000; *Anderson et al.*, 2001; *Phillips et al.*, 2001], and that volcanism on Tharsis waned through the Hesperian but continued to recent times [*Anderson et al.*, 2001; *Hartmann and Neukum*, 2001]. It has been suggested that most of Tharsis volcanism was caused by a shallow mantle upwelling induced by an impact-related buoyancy perturbation [*Reese et al.*, 2004] associated with the dynamic adjustment that occurs during the "flattening stage" (see section 4). However, a recent inversion of gravity and topography used to reconstruct the isostatic crustal root that formed prior to volcanic loading does not reveal an impact basin beneath Tharsis [*Andrews-Hanna et al.*, 2008]. Numerous studies have suggested that a long-lived deep mantle plume or plumes constructed the bulk of this province [e.g., *Harder and Christensen*, 1996; *Kiefer*, 2003].

[87] One of the interesting applications of our work concerns the interaction between deep mantle plumes (constructing Tharsis) and a spreading current (from a Borealis impact), and which is based upon the description in section 4, illustrated in Figure 7. First, if the plume has reached the lithosphere before the spreading current arrives, then it is deflected southward by the spreading flow. This will cause the locus of magmatism to migrate southward until flux in the plume is suppressed and magmatism is halted for some time. As the intensity of the spreading flow diminishes, the plume begins to right itself, so that magmatism resumes and its locus migrates northward toward the [planimetric] position of its root. Meanwhile, if the return flow is significant (along the base of the mantle), the root will have been displaced northward as well. When the plume has straightened completely, its flux is greatest and magmatism is most intense. If instead the plume emerges while the spreading flow is underway, then the first step in this process does not occur; that is, magmatism begins in the south and intensifies while the plume is righted and the locus of magmatism migrates north. *Anderson et al.* [2001] observed a migration northward from the Noachian to the late Hesperian of primary centers of tectonic activity on the Tharsis rise. In that study, the density function from which primary and secondary centers were derived has a marked north-south elongation during the Noachian. These observations, in light of the foregoing discussion, at least recommend the possibility that construction at Tharsis was influenced by a southward spreading flow. As the spatial-temporal development of the Tharsis rise is illuminated by future work, it may be useful to consider this hypothesis alongside others.

[88] Bearing in mind the difficulties of applying our results to the case of three-dimensional spreading flows, our models at least suggest that spreading currents associated with very large perturbations can cause magmatism far outside the boundaries of an impact basin. Three of the largest regions mapped by *Scott and Tanaka* [1986] and *Greeley and Guest* [1987] interpreted as effusive, plains-forming lava flows, are adjacent to two of three major impact basins in the southern highlands. Hellas is bordered by the early Hesperian ridged plains unit (Hr) and its correlates (the Amphitrites Formation (Had) and ridged plains floor unit (Hh2)) to the southwest and northeast, while Isidis is adjacent to the late Hesperian flows of Syrtis Major. Since Hellas formed at the beginning of the Noachian, if the adjacent igneous provinces are related to the flattening and spreading of an impact-induced buoyancy perturbation, this would require long time scales of dynamic adjustment and spreading. The Argyre basin, while not adjacent to any large igneous provinces, contains extensive outcroppings of the "smooth unit" (Hpl3), also associated with lava flows.

[89] The distribution of early Hesperian plains-forming flows in the southern highlands indicates the global extent of early Hesperian volcanism, which possibly also resurfaced the northern lowlands at the same time [*Frey et al.*, 2002; *Head et al.*, 2002]. Volcanism associated with the spreading

stage might express a clear chronological progression, since the youngest magmatism occurs in the farthest reaches of the spreading flow. By contrast, recovery-stage magmatism onsets in patches throughout the spreading region at approximately the same time, as mantle convection resumes and the large-scale circulation pattern is reorganized. Going forward, as a more detailed chronology for early Mars is sorted out, it may be useful to consider whether early Hesperian resurfacing might be related to the recovery stage magmatism of a spreading current with global reach. If related to the Borealis impact of the preNoachian, this would require low Rayleigh number convection for this period in Mars' history.

10. Conclusions

[90] The following results apply to the evolution of temperature and velocity field solutions of the equations of motion for a convecting layer of incompressible fluid with uniform viscosity in the limit of infinite Prandtl number following the insertion of thermal perturbations, and obtained using a finite element numerical calculation that assumes a 2-D Cartesian geometry. The case of two upper boundary conditions (stress-free and no-slip) and heat sources (100% volumetric heating and 100% bottom heating) were examined.

[91] 1. Small, low-temperature perturbations are promptly halted and swept into nearby downflows, and have almost no effect on the ambient flow field. Large, high-temperature perturbations rapidly flatten and cool, and then spread along the upper boundary as a viscous gravity current. This spreading motion drives a large-scale double-roll flow pattern which has the following properties and consequences: (1) Downwellings are swept away or destroyed. (2) The upper and lower boundaries are stabilized so that new downwellings and plumes do not form, which along with mechanism 1 causes convection to cease locally. (3) Plumes are pushed to the center of the spreading region where they sometimes coalesce. The spreading flow is eventually halted by downwellings, at which time new instabilities emerge in both thermal boundary layers and convection resumes, reorganizing the flow field. The postimpact evolution implies two magmatic episodes with distinct temporal and spatial distributions, and with different source regions in the mantle (see section 4).

[92] 2. The time scale t_s in which the perturbation spreads along the upper boundary until it is slowed down and halted by a convective downwelling, can be expressed as a function of the Rayleigh number $Ra_{(H)}$, the dimensionless perturbation size ($\Lambda \equiv \lambda_p/\lambda_m$) and temperature ($\Theta \equiv \Delta T_p/\Delta T_c$):

$$t_s = K_0 \Theta^{\alpha} \Lambda^{\beta} Ra_{(H)}^{\gamma} \tag{24}$$

where $\beta \approx 1$ for both boundary conditions and heat sources, $\gamma \approx -0.5$ for bottom heating (both boundary conditions) and $\gamma \approx -0.13$ for volumetric heating (internal-heating Rayleigh number) and a stress-free upper boundary. Estimates of the exponent α range from 0.3 to 0.4 for the case of a stress-free upper boundary, and from 0.33 to 0.62 for the case of a no-slip upper boundary.

[93] 3. The globally averaged mantle velocity is depressed three standard deviations below its temporal mean value (prior to anomaly insertion) for all perturbations $\Theta\Lambda^3 \geq \Upsilon_{\text{crit}}$, where $\Upsilon_{\text{crit}} = C_0 Ra^{-q}$ for $0 < q < 1$. The values of C_0 and q have been determined for both upper boundary conditions and heat sources considered in this study (see Figure 16). This condition implies that low Ra convection is relatively robust with respect to spatially localized thermal perturbations of a given magnitude, also confirmed in time-lapse snapshots of the temperature and velocity field for low Ra convection. For perturbations of a given size, and assuming ΔT_c increases linearly with Ra, the perturbation temperature ΔT_p must increase only as a fractional power of the convective driving temperature ΔT_c to have the same effect on the globally averaged velocity, i.e., $(\Delta T_p)_{\text{crit}} \sim \Delta T_c^{(1-q)}$.

[94] The following conclusions apply to the estimates of shock heating: The simple "foundering shock" method outlined in section 2 and described in section 5 of the auxiliary material (where other methods are also discussed) provides an effective estimate of the shock heating that results from vertical hypervelocity impacts at great depths in terrestrial mantles. This is accomplished by (1) assuming that release occurs along the Hugoniot; (2) expressing the amount of shock heating in terms of the peak shock pressure (equation (10)); (3) substituting for peak shock pressure the difference between a power law shock pressure decay and lithostatic pressure (as a function of depth), and substituting for ρ_0 the mantle reference model density (as a function of depth). The errors in this approach do not exceed the uncertainties associated with peak shock pressure decay law exponents for the range of material properties reported by *Pierazzo et al.* [1997]. For estimating the characteristic perturbation temperature ΔT_p (the difference between solidus and geotherm) and size (the depth at which shock heating decays to a value below ΔT_p), the error associated with the aforesaid approximation accounts for a slight overestimation of the characteristic perturbation size.

Notation

α	Exponent of Θ in equation (17).
β	Exponent of Λ in equation (17).
γ	Grüneisen parameter (in auxiliary material).
γ	Exponent of Ra in equation (17).
λ_p	Characteristic length scale of type II perturbation.
λ_m	Thickness of convecting layer (mantle).
Λ	λ_p/λ_m.
Θ	$\Delta T_p/\Delta T_c$.
ρ	Mantle density.
σ_v	Preimpact temporal standard deviation about $\bar{v}$.
Υ	Perturbation magnitude: $\Upsilon \equiv \Theta\Lambda^3$.
Υ_{crit}	Critical perturbation magnitude for global stagnation.
C	Intercept of linear shock EOS in U-u space.
C_p	Specific heat at constant pressure.
C_v	Specific heat at constant volume.
d_c	Depth of center of isobaric core.
E_j	Specific internal energy of state j.
n	Shock pressure decay exponent (equation (5)).
n_-	Most gradual decay law exponent for P_s (equation (9)).

n_+	Steepest decay law exponent for P_s (equation (7)).
n_0	Mean decay law exponent for P_s (equation (8)).
P_c	Isobaric core pressure.
P_{ls}	Lithostatic (ambient) pressure.
P_s	Peak shock pressure.
R	Projectile radius.
Ra	Bottom-heating Rayleigh number.
Ra_H	Internal-heating Rayleigh number.
$Ra_{(H)}$	Rayleigh number (internal-heating or bottom-heating).
r_c	Isobaric core radius.
S	Slope of linear shock EOS in U-u space.
$t_{\rm lev}$	Leveling time scale.
t_s	Spreading time scale.
t_{s1}	Spreading time scale estimate derived from $t_{\rm stag}$.
t_{s2}	Spreading time scale estimate derived from $t_{\rm lev}$.
$t_{\rm stag}$	Stagnation time scale.
T_m	Solidus temperature.
ΔT_s	Shock-induced temperature increase.
$\Delta T_{\rm ad}$	Adiabatic contribution to geotherm.
ΔT_c	Convective driving temperature.
ΔT_p	Characteristic temperature of type II perturbation.
u	Particle velocity.
U	Shock front velocity.
v	Globally averaged mantle velocity.
v_i	Projectile vertical incident velocity.
$v_{\rm stag}$	Stagnation velocity.
$\bar{v}$	Preperturbation temporal average of v.
CMB	Core-mantle boundary.
EOS	Equation of state.
IC	Isobaric core.
PIA	Planar impact approximation.
STP	Standard temperature and pressure.
TBL	Thermal boundary layer.

[95] **Acknowledgments.** We are grateful to Sarah Stewart-Mukhopadhyay and Jeffrey Andrews-Hanna for very helpful conversations and suggestions. We would like to thank Francis Nimmo and Chris Reese for insightful reviews that have markedly improved the manuscript. This work was supported by the NASA/Planetary Geology and Geophysics Program.

References

Abbott, D., and A. E. Isley (2002), Extraterrestrial influences on mantle plume activity, *Earth Planet. Sci. Lett.*, *202*, 551–561.

Acuña, M., et al. (1999), Global distribution of crustal magnetization discovered by the Mars Global Surveyor MAG/ER experiment, *Science*, *284*, 790–793.

Ahrens, T. J., and J. D. O'Keefe (1977), Equations of state and impact-induced shock-wave attenuation on the moon, in *Impact and Explosion Cratering*, edited by D. J. Roddy, R. O. Pepin, and R. B. Merrill, pp. 639–656, Pergamon, Elmsford, N. Y.

Anderson, R., J. Dohm, M. Golombek, A. Haldemann, B. Franklin, K. Tanaka, J. Lias, and B. Peer (2001), Primary centers and secondary concentrations of tectonic activity through time in the western hemisphere of Mars, *J. Geophys. Res.*, *106*, 20,563–20,585.

Andrews-Hanna, J., M. Zuber, and W. Banerdt (2008), The borealis basin and the origin of the Martian crustal dichotomy, *Nature*, *453*, 1212–1215.

Arkani-Hamed, J., and A. Pentecost (2001), On the source region of the lunar mare basalt, *J. Geophys. Res.*, *106*, 14,691–14,700.

Banerdt, W., and M. Golombek (2000), Tectonics of the Tharsis region of Mars: Insights from MGS topography and gravity, *Lunar Planet. Sci.*, *XXXI*, Abstract 2039.

Bercovici, D., and A. Kelly (1997), The non-linear initiation of diapirs and plume heads, *Phys. Earth Planet. Inter.*, *101*, 119–130.

Breuer, D., D. A. Yuen, T. Spohn, and S. Zhang (1998), Three dimensional models of Martian mantle convection with phase transitions, *Geophys. Res. Lett.*, *25*, 229–232.

Elkins-Tanton, L., and B. Hager (2005), Giant meteoroid impacts can cause volcanism, *Earth Planet. Sci. Lett.*, *34*, 219–232.

Frey, H., J. Roark, K. Shockey, E. Frey, and S. Sakimoto (2002), Ancient lowlands on Mars, *Geophys. Res. Lett.*, *29*(10), 1384, doi:10.1029/2001GL013832.

Gault, D. E., and E. Heitowit (1963), The partition of energy for hypervelocity impact craters formed in rock, paper presented at 6th Hypervelocity Impact Symposium, Firestone Tire and Rubber Co., Cleveland, 30 Apr. to 2 May.

Ghods, A., and J. Arkani-Hamed (2007), Impact-induced convection as the main mechanism for formation of lunar mare basalts, *J. Geophys. Res.*, *112*, E03005, doi:10.1029/2006JE002709.

Greeley, R., and J. Guest (1987), Geologic map of the eastern equatorial region of Mars, scale 1:15,000,000, *U.S. Geol. Surv. Map*, *I-1802B*.

Green, D. H. (1972), Archaean greenstone belts may include terrestrial equivalents of lunar maria?, *Nature*, *15*, 263–270.

Harder, H., and U. R. Christensen (1996), A one-plume model of Martian mantle convection, *Nature*, *380*, 507–509.

Hartmann, W., and G. Neukum (2001), Cratering chronology and the evolution of Mars, *Space Sci. Rev.*, *96*, 164–194.

Head, J., M. Kreslavsky, and S. Pratt (2002), Northern lowlands of Mars: Evidence for widespread volcanic flooding and tectonic deformation in the Hesperian period, *J. Geophys. Res.*, *107*(E1), 5003, doi:10.1029/2000JE001445.

Howard, L. (1966), Convection at high Rayleigh number, *Appl. Mech., Proc. Int. Cong. 11th*, 1109–1115.

Huppert, H. (1982), The propagation of two-dimensional and axisymmetric viscous gravity currents over a rigid horizontal surface, *J. Fluid Mech.*, *121*, 43–58.

Ivanov, B. A., and H. J. Melosh (2003), Impacts do not initiate volcanic eruptions: Eruptions close to the crater, *Geology*, *31*(10), 869–872.

Jones, A. P., G. D. Price, N. J. Price, P. S. DeCarli, and R. A. Clegg (2002), Impact induced melting and the development of large igneous provinces, *Earth Planet. Sci. Lett.*, *202*, 551–561.

Kiefer, W. (2003), Melting in the Martian mantle: Shergottite formation and implications for present-day mantle convection on Mars, *Meteorit. Planet. Sci.*, *39*, 1815–1832.

King, S. D., A. Raefsky, and B. H. Hager (1990), Conman: Vectorizing a finite element code for incompressible two-dimensional convection in the Earth's mantle, *Phys. Earth Planet. Inter.*, *59*, 195–207.

Lister, J., and R. Kerr (1989), The propagation of two-dimensional and axisymmetric viscous gravity currents at a fluid interface, *J. Fluid Mech.*, *203*, 215–249.

Loper, D. E. (1991), Mantle plumes, *Tectonophysics*, *187*, 373–384.

Manga, M., and J. Arkani-Hamed (1991), Remelting mechanisms for shallow source regions of mare basalts, *Phys. Earth Planet. Inter.*, *68*, 9–31.

Marinova, M., O. Aharonson, and E. Asphaug (2008), Mega-impact formation of the Mars hemispheric dichotomy, *Nature*, *453*, 1216–1219.

McQueen, R. G. (1991), Shock waves in condensed media: Their properties and the equation of state of materials derived from them, in *Equazioni di stato ad alta pressione: Teoria e applicazioni*, edited by S. Eliezer and R. Ricci, pp. 101–313, Scuola Internazionale di Fisica Enrico Fermi, Società Italiana di Fisica, Bologna, Italy.

Melosh, M. J. (1989), *Impact Cratering: A Geological Process*, 1st ed., Oxford Univ. Press, New York.

Monteux, J., N. Coltice, F. Dubuffet, and Y. Ricard (2007), Thermo-mechanical adjustment after impacts during planetary growth, *Geophys. Res. Lett.*, *34*, L24201, doi:10.1029/2007GL031635.

Muller, R. A. (2002), Avalanches at the core-mantle boundary, *Geophys. Res. Lett.*, *29*(19), 1935, doi:10.1029/2002GL015938.

Nimmo, F., S. Hart, D. Korycansky, and C. Agnor (2008), Implications of an impact origin for the Martian hemispheric dichotomy, *Nature*, *453*, 1220–1223.

Olson, P., G. Schubert, and C. Anderson (1987), Plume formation in the D″-layer and the roughness of the core-mantle boundary, *Nature*, *327*, 409–413.

Phillips, R., et al. (2001), Ancient geodynamics and global-scale hydrology on Mars, *Science*, *291*, 2587–2591.

Pierazzo, E., A. M. Vickery, and H. J. Melosh (1997), A reevaluation of impact melt production, *Icarus*, *127*, 408–423.

Press, W. H., S. A. Teukolsky, W. T. Vetterling, and B. P. Flannery (1988), *Numerical Recipes in C*, 2nd ed., Cambridge Univ. Press, Cambridge, U. K.

Reese, C. C., and V. S. Solomatov (1999), Non-newtonian stagnant lid convection and magmatic resurfacing of Venus, *Icarus*, *139*, 67–80.

Reese, C. C., and V. S. Solomatov (2006), Fluid dynamics of local Martian magma oceans, *Icarus*, *184*, 102–120.

Reese, C. C., V. S. Solomatov, J. R. Baumgardner, D. R. Stegman, and A. V. Vezolainen (2004), Magmatic evolution of impact-induced Martian mantle plumes and the origin of tharsis, *J. Geophys. Res.*, *109*, E08009, doi:10.1029/2003JE002222.

Richter, F. (1973), Convection and the large-scale circulation of the mantle, *J. Geophys. Res.*, *78*, 8735–8745.
Schmerr, C., Y. Fei, and C. Bertka (2001), Extending the solidus for a model iron-rich Martian mantle composition to 25 GPa, *Lunar Planet. Sci.*, *XXXII*, Abstract 1157.
Schubert, G., and T. Spohn (1990), Thermal history of Mars and the sulfer content of its core, *J. Geophys. Res.*, *95*, 14,095–14,104.
Schubert, G., D. Turcott, and P. Olson (2001), *Mantle Convection in the Earth and Planets*, 1st ed., Cambridge Univ. Press, Cambridge, U. K.
Schultz, P. H., and D. E. Gault (1975), Seismic effects of major basin formation on the moon and mercury, *Moon*, 159–177.
Scott, D. H., and K. L. Tanaka (1986), Geological map of the western equatorial region of Mars, *U.S. Geol. Surv. Map*, *I-1802A*.
Solomatov, V. (1995), Scaling of temperature- and stress-dependent viscosity convection, *Phys. Fluids*, *7*, 266–274.
Spohn, T., F. Sohl, and D. Breuer (1998), Mars, *Astron. Astrophys. Rev.*, *8*, 181–286.
Stacey, F. D. (1992), *Physics of the Earth*, 3rd ed., Brookfield, Queensland, Australia.
Stevenson, D. (2001), Mars' core and magnetism, *Nature*, *412*, 214–219.
Stevenson, D., T. Spohn, and G. Schubert (1983), Magnetism and thermal evolution of the terrestrial planets, *Icarus*, *54*, 466–489.
Tonks, W. B., and H. J. Melosh (1993), Magma ocean formation due to giant impacts, *J. Geophys. Res.*, *98*, 5319–5333.
Wetherill, G. W. (1990), Formation of the Earth, *Ann. Rev. Earth Planet. Sci.*, *18*, 205–256.
Whitehead, J. (1975), Dynamics of laboratory diapir and plume models, *J. Geophys. Res.*, *80*, 705–717.
Williams, D. A., and R. Greeley (1994), Assessment of antipodal-impact terrains on Mars, *Icarus*, *110*, 196–202.
Yoder, C., A. Konopliv, D. Yuan, E. Standish, and W. Folkner (2003), Fluid core size of Mars from detection of the solar tide, *Science*, *300*, 299–303.
Zerr, A., A. Diegeler, and R. Boehler (1998), Solidus of Earth's deep mantle, *Science*, *281*, 243–246.

B. H. Hager, W. A. Watters, and M. T. Zuber, Department of Earth, Atmospheric, and Planetary Sciences, Massachusetts Institute of Technology, 77 Massachusetts Ave., Cambridge, MA 02139, USA. (watters@mit.edu)